Drug Delivery and Translational Research
https://doi.org/10.1007/s13346-023-01440-6

ORIGINAL ARTICLE

Enhanced oral delivery of hesperidin-loaded sulfobutylether-β-cyclodextrin/chitosan nanoparticles for augmenting its hypoglycemic activity: in vitro-in vivo assessment study

Mona Ebrahim Elmoghayer[1] · Noha Mohamed Saleh[1] · Irhan Ibrahim Abu Hashim[1]

Accepted: 26 September 2023

Abstract
Hesperidin (Hsd), a bioactive phytomedicine, experienced an antidiabetic activity versus both Type 1 and Type 2 *Diabetes mellitus*. However, its intrinsic poor solubility and bioavailability is a key challenging obstacle reflecting its oral delivery. From such perspective, the purpose of the current study was to prepare and evaluate Hsd-loaded sulfobutylether-β-cyclodextrin/chitosan nanoparticles (Hsd/CD/CS NPs) for improving the hypoglycemic activity of the orally administered Hsd. Hsd was first complexed with sulfobutylether-β-cyclodextrin (SBE-β-CD) and the complex (CX) was found to be formed with percent complexation efficiency and percent process efficiency of 50.53 ± 1.46 and 84.52 ± 3.16%, respectively. Also, solid state characterization of the complex ensured the inclusion of Hsd inside the cavity of SBE-β-CD. Then, Hsd/CD/CS NPs were prepared using the ionic gelation technique. The prepared NPs were fully characterized to select the most promising one (F1) with a homogenous particle size of 455.7 ± 9.04 nm, a positive zeta potential of + 32.28 ± 1.12 mV, and an entrapment efficiency of 77.46 ± 0.39%. The optimal formula (F1) was subjected to further investigation of in vitro release, ex vivo intestinal permeation, stability, cytotoxicity, and in vivo hypoglycemic activity. The results of the release and permeation studies of F1 manifested a modulated pattern between Hsd and CX. The preferential stability of F1 was observed at 4 ± 1 °C. Also, the biocompatibility of F1 with oral epithelial cell line (OEC) was retained up to a concentration of 100 µg/mL. After oral administration of F1, a noteworthy synergistic hypoglycemic effect was recorded with decreased blood glucose level until the end of the experiment. In conclusion, Hsd/CD/CS NPs could be regarded as a hopeful oral delivery system of Hsd with enhanced antidiabetic activity.

Keywords Hesperidin · Hypoglycemic · Sulfobutylether-β-cyclodextrin · Chitosan · Nanoparticles · Release · Permeation

Introduction

Hesperidin (Hsd) (30,5,7-trihydroxy 40-methoxy flavanone 7-rutinoside) is a phytomedicine that is found plentifully in citrus fruits, such as oranges, mandarins, lemons, limes, and grapefruits (Fig. 1A) [1, 2]. It is a fundamental flavanone glycoside in the peel of sweet oranges [2–4]. Hsd has been identified as a promising phytoconstituent with antibacterial, hypolipidemic, antiallergic, antihypertensive, cardioprotective, and anticancer properties [5–7]. Additionally, it has shown a potent antioxidant activity which helps to safeguard against various chronic diseases such as *Diabetes mellitus* [2, 8]. Hsd depicts auspicious antidiabetic action as it improves insulin sensitivity, and therefore prevents hyperglycemia in both Type 1 and Type 2 diabetes [9–11]. It was also reported that Hsd had protective effects against diabetic nephropathy and neuropathy [12, 13]. Despite the hopeful therapeutic outcomes of Hsd, its poor aqueous solubility, and bioavailability have limited its oral delivery [14, 15]. Thus, an approach that could enhance the solubility of Hsd such as complexation might be helpful to improve its dissolution, bioavailability, stability, and biological activity [1]. Also, the loading of Hsd in bioactive polymer-based (NPs) would provide an innovative delivery system for further enrichment of the in vivo bioactivity.

Beta-cyclodextrin (β-CD) is a cyclic oligosaccharide consisting of seven D-glucopyranose units connected by 1,4-glucosidic bonds [16–18]. β-CDs have a central hydrophobic

✉ Noha Mohamed Saleh
nunu_ramy@mans.edu.eg

[1] Department of Pharmaceutics, Faculty of Pharmacy, Mansoura University, Mansoura 35516, Egypt

Published online: 16 October 2023

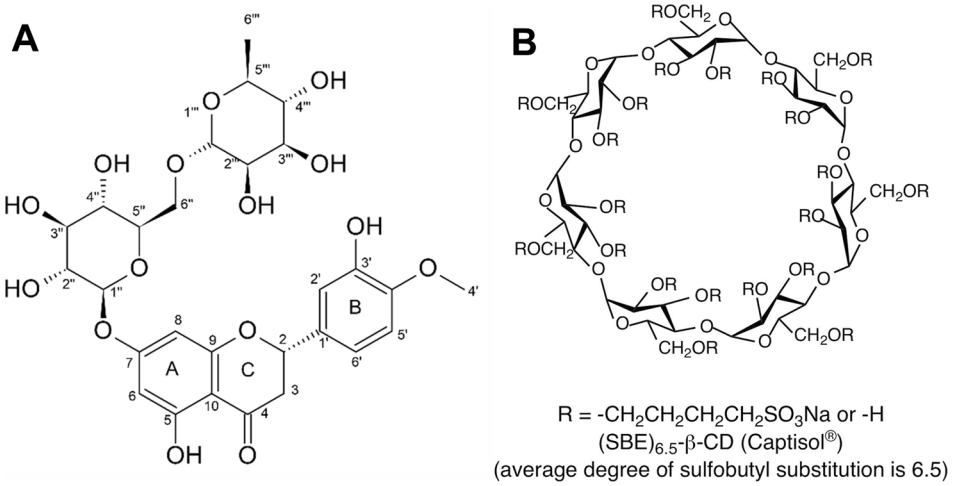

Fig. 1 Chemical structures of hesperidin (**A**) [2] and sulfobutylether-ß-cyclodextrin (**B**) [162]

cavity and outer hydrophilic surface, enabling them to encapsulate lipophilic drugs [19–21]. A modification of β-CDs via the addition of sulfobutyl moiety to form sulfobutylether-β-CD (SBE-β-CD, Fig. 1B) shows greatly enhanced aqueous solubility, permeability, bioavailability, biocompatibility, low toxicity, and amended complexing ability for lipophilic drugs compared to the parent β-CD [22–24].

Chitosan (CS) is a natural bioactive linear polysaccharide with N-acetyl glucosamine units linked with glucosamine ones by β-1,4-glucosidic bonds [25–27]. CS demonstrated versatile pharmacological activities such as anti-diabetic, antioxidant, anti-allergic, anti-inflammatory, anticoagulant, antibacterial, and antiviral activities [28, 29]. The ionic gelation of CS with polyanions as SBE-β-CD is one of the most popular and simple approaches for the formulation of NPs. The negatively charged sulfonate groups of SBE-β-CD crosslink with the positively charged amino groups of CS in an environment-friendly non-organic aqueous medium [30, 31]. CS has a unique feature of bearing a positive charge unlike other polysaccharides, allowing it to interact and bind strongly with negatively charged biological surfaces [32, 33]. Moreover, CS NPs improve drug penetration, safeguard acid-sensitive medicines, boost drug release in basic pH, and offer excellent oral bioavailability [34, 35]. Interestingly, CS-based NPs are promising carriers for the delivery and complementation of antidiabetic drugs [36].

To the best of our knowledge, limited trials have been conducted to increase the solubility of Hsd via complexation. At the same time, few studies reported the heightened antidiabetic activity of Hsd NPs [37–39]. Hence, this study is the first one aimed to enhance the solubility of Hsd by its complexation with SBE-β-CD. Then, our effort focused on the development of CS-based NPs via the ionic gelation technique to serve as an oral delivery system of Hsd for augmenting its hypoglycemic activity.

Materials and methods

Materials

CS (Mwt 50-190 kDa, deacetylation percent 85%) and porcine stomach mucin were purchased from Sigma-Aldrich (Saint Louis, MO, USA). Hsd was obtained from Abcam (Cambridge, MA, USA). SBE-β-CD sodium salt; Captisol® (Mwt 2160) was kindly supplied by Cydex L.C. (USA). Millipore filters were obtained from Millipore Corporation (Bedford, MA 01730, USA). Oral epithelial cell (OEC) was gotten from Nawah Scientific Inc., (Mokatam, Cairo, Egypt). Glucose TR oxidase peroxidase kit (GOD/POD) was bought from Spinreact, S.A.U., Spain. Other chemicals were of analytical grades and were used without additional treatment.

Methodology

Phase solubility

An excess amount of Hsd was added to SBE-β-CD aqueous solutions (0.0–3 mM) in 10-mL screw-capped tubes. The tubes were placed in a thermostatic shaker bath for 24 h at 25 ± 0.5 and 37 ± 0.5 °C (Grant Instrument, Cambridge Ltd., UK) [40–42]. Then, the tubes were centrifuged for 1 h at 10,000 rpm (Centrifuge, Hettich Micro 22 R, Germany). An aliquot (3 mL) of the supernatant was filtered (0.45 µm) and measured spectrophotometrically at 284 nm after proper dilution (UV/VIS spectrophotometer, JASCO, Tokyo, Japan). The phase solubility curve of Hsd (mM) versus SBE-β-CD (mM) was constructed and the slope was calculated. The stability constant ($K_{1:1}$) of the Hsd/SBE-β-CD inclusion complex (CX) was determined as follows [43, 44]:

$$K_{1:1} = \frac{\text{Slope}}{S_0(1 - \text{Slope})} \quad (1)$$

where S_0 is the intrinsic solubility of Hsd in the absence of SBE-β-CD.

Preparation of Hsd/SBE-β-CD complex (CX) and physical mixture

The inclusion complex of SBE-β-CD with Hsd was prepared by the freeze-drying technique with some modifications [45]. First, SBE-β-CD (54.1 mg) was dissolved in 25 mL distilled water. Hsd (15.3 mg) was dissolved in 18 mL methanol using water bath sonication for 10 min (Sonix IV, model ss101H230, USA). Then, the aqueous solution of SBE-β-CD was dropped quickly onto the Hsd solution under magnetic stirring (Misung Scientific Co. model MS-300HS, Ltd, Korea). The obtained mixture was shaken for 48 h at 37 °C (GFL Gesellschaft für Labortechnik, Burgwedel, Germany). After that, the clear mixture was freeze-dried for 24 h (Freeze dryer, SIM FD8-8T, SIM International, USA), and the dried CX was collected, weighed, and kept for further evaluation. A physical mixture of Hsd and SBE-β-CD was prepared in a 1:1 molar ratio by gently mixing the two components [46].

Characterization of Hsd/SBE-β-CD complex (CX)

Percent complexation and process efficiency The freeze-dried CX (5 mg) was solubilized in 2.5 mL distilled water (to dissolve the complexed Hsd only) and another 5 mg of the CX was dissolved in 2.5 mL methanol (to dissolve total Hsd (both free and complexed Hsd)). Then, both solutions were sonicated in a water bath sonicator for 10 min. The obtained solutions were filtered to remove the undissolved Hsd. After proper dilution, the Hsd concentration in water (complexed Hsd) and methanol (total Hsd (free and complexed)) was measured spectrophotometrically at 284 nm [47]. Also, the yield of the CX or process efficiency was stated as the percentage of the mass of the recovered CX (lyophilized powder) over the sum mass of the initial components (Hsd + SBE-β-CD). The percent complexation efficiency (%CE) and the percent process efficiency (%PE) were calculated as follows [48, 49]:

$$\%CE = \frac{\text{Complexed Hsd}}{\text{Total Hsd}} \times 100 \quad (2)$$

$$\%PE = \frac{\text{wt of Cx}}{\text{wt of Hsd} + \text{wt of SBE} - \beta - \text{CD}} \times 100 \quad (3)$$

Fourier transform-infrared (FT-IR) spectroscopy The FT-IR spectra of Hsd, SBE-β-CD, their binary physical mixture (Ph_{CX}) with the same ratios of Hsd and SBE-β-CD in CX, and CX were determined using FT-IR spectrophotometer (Madison Instruments, Middleton, WI, USA). The analysis was conducted using the KBr technique. Individual samples (2 mg each) were milled with KBr (200 mg), compressed, and analyzed over a range of 4000–500 cm^{-1}.

Differential scanning calorimetry (DSC) Thermograms of Hsd, SBE-β-CD, Ph_{CX}, and CX were obtained utilizing the DSC technique (DSC 6000; Perkin-Elmer, Waltham, MA, USA). The samples were weighed (4 mg each) and heated gradually in aluminum pans under a dry nitrogen stream purging at 20 mL/min. The temperature range and the heating rate were 50–350 °C and 10 °C/min, respectively. For the temperature calibration, indium was applied as a reference standard during DSC runs.

X-ray diffractometry (XRD) X-ray diffraction patterns of Hsd, SBE-β-CD, Ph_{CX}, and CX were recorded using an X-ray diffractometer equipped with Cu Kα (Diano Corp., Woburn, MA, USA). The examination was conducted over a scanning range from 3 to 50° at 2θ angle at a current and a voltage of 9 mA and 45 kV, respectively.

Proton-nuclear magnetic resonance (^{1}H-NMR) ^{1}H-NMR spectra were obtained using a Bruker DRX spectrometer (Bruker Daltonics Inc., MA, USA) at 600 MHz and JEOL ECA 500 II spectrometers (Japan) at 500 MHz, and Bruker Ascend™ 400 spectrometer (Bruker Daltonics, Bremen, Germany) at 400 MHz. The applied solvent was DMSO-d_6. Hsd was accurately weighed (1 mg) and dissolved in 500 µL DMSO, while CX (1 mg) was dissolved in 1 mL DMSO. The obtained data were processed using MestreNova processor software. Chemical shifts were measured in *ppm* on the δ scale regarding the TMS resonance; coupling constants (*J*) were expressed in Hz.

Scanning electron microscopy (SEM) The topographical characteristics of Hsd, SBE-β-CD, Ph_{CX}, and CX were explored using SEM worked at an acceleration voltage of 20 kV (JSM 6150, JEOL, Tokyo, Japan). Individual samples were loaded on stubs. Then, the fixed samples were covered with a gold/palladium alloy with the JFC1200 Fine Coater (JEOL, Tokyo, Japan). The pre-prepared samples were examined and microphotographs were acquired at a suitable magnification.

Preparation of hesperidin/sulfobutylether-β-cyclodextrin/chitosan nanoparticles (Hsd/CD/CS NPs)

As reported, it was essential to perform preliminary trials of blank NPs preparation by ionotropic gelation method to detect NPs formation zone as a prerequisite step for medicated NPs

fabrication with optimum characteristics [50, 51]. Thus, solutions of SBE-β-CD and CS at a concentration range of 0.25 to 2% w/v were prepared. SBE-β-CD and CS were dissolved in distilled water and acetic acid aqueous solution (1% v/v), respectively. The SBE-β-CD solution was transferred into a syringe and added in a dropwise manner to the CS solution (20 mL) at room temperature till the clear solution turned opaque (formation of NPs) [52]. This phase transition was identified as the formation of NPs. Based on the obtained finding, CS at the concentration of 0.5% w/v (5 mg/mL) was chosen for the preparation of all the coming NPs due to its ease of handling, suitable viscosity, and lack of clumping.

In this study, the formulation of Hsd/CD/CS NPs passed through two steps. The first one was to prepare CX by the above-mentioned method. Then, the CX was dissolved in deionized water (DIW) at a concentration of 10 mg/mL. The CX solution was gradually dropped into 10 mL of CS solution (5 mg/mL) till the clear solution turned opaque [53]. The NPs were separated by cooling centrifugation (Acculab CE16-4X100RD, USA) at 13,000 rpm for 2 h. The obtained cakes were collected, freeze-dried, and kept for further evaluation. In the same manner, plain CD/CS NPs were prepared but by using a pure SBE-β-CD solution instead of the CX one. The constituents of the prepared NPs are listed in Table 1.

Characterization of Hsd/CD/CS NPs

Hsd entrapment efficiency The entrapment efficiency percentage (EE%) was assessed indirectly. The unentrapped Hsd (free Hsd) in Hsd/CD/CS NPs dispersion was separated by cooling centrifugation at 13,000 rpm for 2 h. Then, the supernatant was quantified spectrophotometrically at 284 nm versus the corresponding supernatant of the plain CD/CS NPs as a blank after proper dilution. The EE% was calculated as follows [54, 55]:

$$EE\% = \frac{Hsd_t - Hsd_f}{Hsd_t} \times 100 \quad (4)$$

Table 1 The compositions of Hsd/CD/CS nanoparticles

Formula	CS:CX	CS (mg)	SBE-β-CD equivalent amount (mg) in CX
F1	1:1.5	50	75 mg
F2	1:1.25	50	62.5 mg
F3	1:1	50	50 mg
F4	1:0.8	50	40 mg
F5	1:0.67	50	33.5 mg

CS chitosan *SBE-β-CD* sulfobutylether-β-cyclodextrin, *CX* Hsd/SBE-β-CD complex

where Hsd_t is the total of Hsd and Hsd_f is the unentrapped Hsd in the supernatant.

Particle size, polydispersity index, and zeta potential After proper dilution with DIW, the particle size, polydispersity index (PDI), and zeta potential (ZP) of Hsd/CD/CS NPs were measured using Malvern Zetasizer Nano ZS (Malvern Instruments Limited, UK). Dynamic Light Scattering (DLS) and Laser Doppler Micro-Electrophoresis procedures were employed for particle size and ZP measurements, respectively.

Mucoadhesive strength The assessment of the mucoadhesive strength of Hsd/CD/CS NPs was related to the electrostatic attraction between mucin (negatively charged) and NPs (positively charged) [56]. Equal volumes of NPs dispersion and mucin solution (0.5 mg/mL) in phosphate buffer saline (pH 7.4) were magnetically stirred for 1 h at 37 °C. Then, the obtained mixture was centrifuged at 11,000 rpm for 1 h (Benchtop Centrifuge, Sigma Laborzentrifugen GmbH, Germany). The total mucin (before interaction with the NPs) and the free one (in the supernatant) were measured spectrophotometrically at 251 nm [32, 57, 58]. The mucoadhesive strength of Hsd/CD/CS NPs expressed as mucin binding efficiency (%) was calculated as follows:

$$\text{Mucin binding efficiency } (\%) = \frac{Mucin_t - Mucin_f}{Mucin_t} \times 100 \quad (5)$$

where $Mucin_t$ is the total mucin and $Mucin_f$ is the free mucin in the supernatant.

Based on the characterization of Hsd/CD/CS NPs, an optimized formula (F1) was selected to undergo further investigations.

Characterization of the optimal formula (F1)

Transmission electron microscopy (TEM) The morphological characteristics of F1 were observed by TEM (JEOL 2100; JEOL, Tokyo, Japan). A drop of a fresh F1 dispersion was spread over a carbon-coated copper grid and then extra dispersion was removed by a filter paper. The sample was allowed to dry at room temperature and directly inspected without staining. The microphotographs were captured at proper magnification.

SEM The topography of CX, CS, physical mixture of CX and CS (Ph_{NPs}), and F1 was investigated using SEM operated at an acceleration voltage of 20–30 kV. The sample preparation was conducted as mentioned before under the "Scanning electron microscopy (SEM)" section.

Solid state characterization The FT-IR spectra, DSC thermograms, and X-ray diffraction patterns of CX, CS, and Ph_{NPs} as well as the freeze-dried samples of F1 and the corresponding plain NPs (PLF1) were measured as mentioned under the "Characterization of Hsd/SBE-β-CD complex (CX)" section.

In vitro release

The in vitro release of Hsd, CX, and F1 was studied using modified vertical Franz diffusion cells with a diffusional surface area of 5.12 cm^2/cell. A dialysis cellulose membrane (Mwt cut off 12,000–14,000 Da, Sigma-Aldrich, Saint Louis, MO, USA) was pre-equilibrated overnight with the release media. Then, donor and receptor half-cells were separated using the cellulose membrane. The methanolic buffered solutions at pH 1.2, 6.8, and 7.4 were applied as release media to simulate the gastric, intestinal, and physiological pH, respectively. Methanol was added at a concentration of (40% v/v) to secure sink conditions throughout the experiment [59]. Briefly, aqueous CX solution, F1 dispersion, and aqueous Hsd dispersion equivalent to 0.7 mg Hsd in DIW were introduced into the donor compartments. The release media (100 mL/cell) were placed in the receptor ones. The Franz cells were placed in a thermostatically controlled incubator kept at 37 ± 0.5 °C and shaken at 100 rpm throughout the experiment (GFL Gesellschaft für Labortechnik, Burgwedel, Germany). During the experiment, samples were withdrawn at predetermined time points and replaced with an equal volume of fresh medium equilibrated at the same conditions. The gathered samples were analyzed spectrophotometrically at 284 nm. Ultimately, the cumulative Hsd released (%) was determined at each time point and plotted versus the corresponding time.

Kinetic analysis

To acquire a comprehensive understanding of the Hsd release mechanism, the release data were fitted to kinetic models that were zero-order (A vs. t), first-order ($\log\left(A_o - A\right)$ vs. t), Higuchi (A vs. $t^{1/2}$) [60], and Korsmeyer-Peppas equation $\left(A_t/A_\infty = k_p t^n\right)$ [61]. Where, A is the cumulative percent Hsd released at time t, $\left(A_o - A\right)$ is the percent of the remaining Hsd after time t, A_t/A_∞ is the fraction of Hsd released after time t, k_p is the Korsmeyer-Peppas kinetic constant, and n is the release diffusional exponent (n = slope of $\log A_t/A_\infty$ vs. $\log t$). The kinetic model having the highest coefficient of determination (R^2) was stated as the Hsd release mechanism [62, 63].

Ex vivo intestinal permeation

An excised goat small intestine was obtained from the local slaughterhouse. The sections of intestinal tissue were freshly isolated, dissected longitudinally, and washed in a series of saline solutions under sterile conditions. Then, the sample tissues were kept in saline at −20 °C until experimenting. The Research Ethical Committee at the Faculty of Pharmacy, Mansoura University permitted protocols involving the excision of the tissue samples and the animal experiments (Ethical Approval Code: 2023-129) following "The Principle of Laboratory Animal Care" (NIH publication No. 85-23, revised 1985). Also, the animal-related experiments were completed in agreement with the Animal Research: Reporting of In Vivo Experiments (ARRIVE) principles.

The ex vivo permeation study was conducted using the modified vertical Franz cell with a diffusional area of 5.12 cm^2/cell. The intestine samples were positioned between the donor and receptor compartments with the inner mucous side facing the donor compartment. The methanolic buffered solution (40% v/v) at pH 7.4 was employed as a permeation medium. Then, the permeation experiment was conducted using the same condition stated under the "In vitro release" section. with Hsd amount equivalent to 0.7 mg in DIW (CX solution, F1 dispersion, and Hsd dispersion) was introduced into the donor compartments. The amount of Hsd permeated across the intestine per unit surface area (dM/A) (μg/cm^2) was plotted versus time. After that, the slope of the linear part of the constructed permeation curve was designated as the steady-state flux (J_{ss}, μg/cm^2.h). The permeability coefficient (K_p, cm/h) was estimated by dividing the J_{ss} over the donor concentration of Hsd (C_0, μg/mL) [64–66].

Stability study

The stability of F1 was studied at refrigerator (4 ± 1 °C) and ambient temperature throughout 6 months [67–69]. Freshly prepared F1 dispersions were stored in amber glass screw-capped bottles at the above-mentioned temperatures. The particle size, PDI, ZP, and drug retention percentage (DR%) of NPs were assessed at zero, 1 month, 3 months, and 6 months. The DR% was calculated as follows [70]:

$$\text{Drug retention (DR\%)} = \frac{\text{EE\% at each time interval}}{\text{EE\% at zero time}} \times 100 \quad (6)$$

where EE% is the Hsd entrapment efficiency percentage inside NPs.

Cytotoxicity assay

Cytotoxicity assay was conducted using a normal oral epithelial cell line (OEC). The water-soluble tetrazolium salt I (WST-1) technique was applied. OEC was preserved in DMEM media enriched with 100 units/mL of penicillin, 100 mg/mL of streptomycin, and 10% of heat-inactivated fetal bovine serum in a humidified atmosphere of 5% (v/v) CO_2 at 37 °C. Aliquots of cell suspension (50 µL, 3×10^3 cells) were cast in 96-well plates and incubated for 24 h in complete media. Then, additional aliquots of 50 µL media containing Hsd, CX, PLF1, and F1 at concentrations of 0.01, 0.1, 1, 10, and 100 µg/mL were added to the cells. The treated cells were incubated for 48 h. After that, cells were further treated with WST-1 (10 µL/well), and the absorbance was measured spectrophotometrically after 1 h at 450 nm using a microplate reader (Allmendgrün, Ortenberg). Percent cell viability (%) was estimated using the absorbance of treated cells and that of the negative control cells. Then, the inhibitory concentration of 50% of cells (IC_{50}) was calculated by plotting percent cell viability versus log concentrations [71, 72].

$$\text{Cell viability (\%)} = \frac{\text{A450 of treated cells}}{\text{A450 of controlled cells}} \times 100 \quad (7)$$

In vivo evaluation of the pharmacodynamic hypoglycemic effect

Fifteen male Sprague-Dawley rats (ca 190–200 g) were used in this study. The Research Ethical Committee at the Faculty of Pharmacy, Mansoura University approved protocols involving the excision of the tissue samples and the animal experiments (Ethical Approval Code: 2023-129) under "The Principle of Laboratory Animal Care" (NIH publication No. 85-23, revised 1985). Also, the animal experiments were performed in agreement with the Animal Research: Reporting of In Vivo Experiments (ARRIVE) principles. Two weeks before the experiment, the animals were adapted to an environmentally monitored room with free access to a standard diet and water ad libitum. Before the experiment, the animals were fasted for 12 h with water ad libitum. At random, the animals were partitioned into three groups (five animals per group):

Group I: Oral Hsd administration.
Group II: Oral administration of Hsd/SBE-β-CD complex (CX).
Group III: Oral administration of Hsd/CD/CS NPs (F1).

Each animal served as its control by determining the blood glucose level in the blood sample that was withdrawn before the oral administration (BG_0). The animals of Group I, II, and III received oral doses of Hsd aqueous dispersion, CX aqueous solution, and F1 dispersion, respectively, equivalent to 50 mg Hsd/kg. Blood samples were collected from the retro-orbital venous plexus at 0, 1, 2, 4, 6, 9, and 12 h after the oral administration [73, 74]. The glucose oxidase/peroxidase method was employed to estimate the blood glucose level (BG_t) using the GOD/POD kit. The percentage reduction in the blood glucose level (%RBGL) was possessed as a reversal for the hypoglycemic response that was calculated as follows [75, 76]:

$$\%\text{RBGL} = \frac{BG_0 - BG_t}{BG_0} \times 100 \quad (8)$$

where BG_0 is the blood glucose at zero time and BG_t is the blood glucose at a certain time interval.

Statistical analysis

In vitro and in vivo data of this study were stated as mean ± standard deviation (SD) and mean ± standard error of the mean (SEM), respectively. Statistical analysis was conducted by one-way analysis of variance (ANOVA) followed by a multiple comparisons test (Tukey-Kramer) using GraphPad Prism software version 8.00 (San Diego, CA, USA). The P values at level $P < 0.05$ were considered statistically significant.

Results and discussion

Characterization of Hsd/SBE-β-CD complex (CX)

Phase solubility

The phase solubility diagram of Hsd in SBE-β-CD solutions at 25 ± 0.5 and 37 ± 0.5 °C is illustrated in Fig. 2. Over the studied concentration range, it could be observed that the solubility of Hsd enhanced linearly with rising the SBE-β-CD concentration. Such a pattern could be specified as AL type based on the theory suggested by Higuchi and Connors [77, 78]. As the slope was less than one (0.02799 and 0.02770 for 25, and 37 °C, respectively), the stoichiometry of the complexation was assumed to be 1:1. The intrinsic solubilities (S_0) of Hsd at 25 and 37 °C were 0.01141 and 0.02313 mM, respectively. Additionally, the stability constant ($K_{1:1}$) values were 2524 and 1232 M^{-1}, at 25 and 37 °C, respectively. The values of $K_{1:1}$ suggested the formation of stable CX as they lay between a range of 200 to 5000 M^{-1} which could improve the solubility, bioavailability, and aqueous stability of poorly soluble drugs. Likewise, the $K_{1:1}$ was observed to decline with raising temperature from 25 to

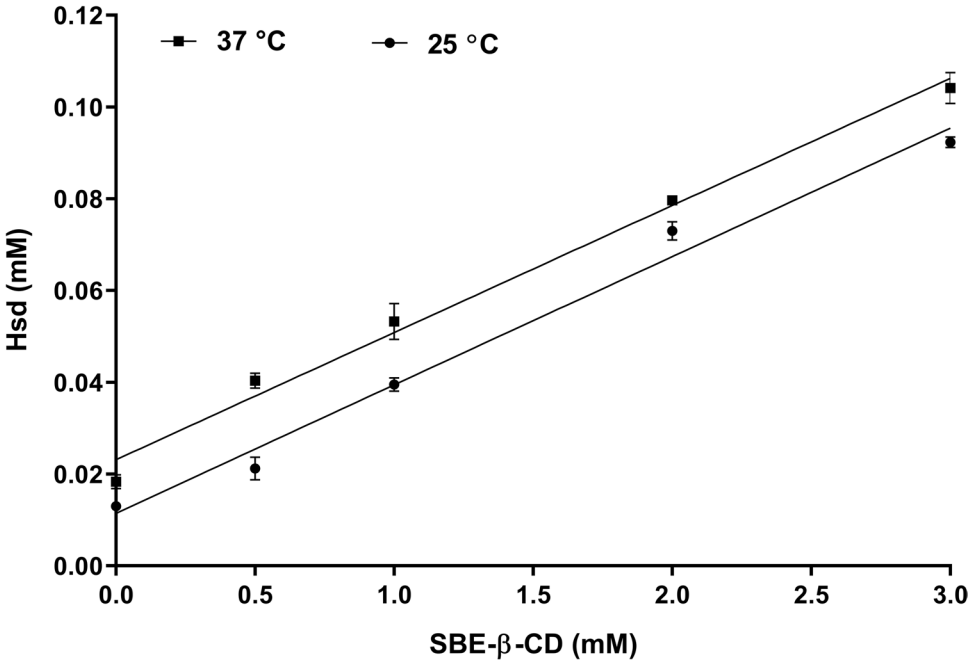

Fig. 2 Phase solubility diagram of Hsd in SBE-β-CD. Each point represents the mean ± SD ($n = 3$). Abbreviations: Hsd, hesperidin and SBE-β-CD, sulfobutylether-β-cyclodextrin

37 °C which indicated that the development of the inclusion complex was a spontaneous exothermic process [79].

Percent complexation and process efficiency

The values of %CE and %PE of the CX were 50.53 ± 1.46 and 84.52 ± 3.16 %, respectively. These findings were consistent with other investigators [49]. The values of %CE and %PE are dependent on the complexation time and temperature [80]. Therefore, it could be supposed that the employed complexation procedure was effective and provided a satisfying %PE value (more than 60%) [81].

FT-IR

Figure 3A illustrates the FT-IR spectra of Hsd, SBE-β-CD, Ph_{CX}, and CX. In the spectrogram of Hsd (a), strong bands of OH at 3542 and 3476 cm^{-1}, CH (aliphatic) at 2979 and 2919 cm^{-1}, C=C (aromatic) at 1609, 1518, and 1444 cm^{-1}, C-O at 1277 and 1204 cm^{-1}, and C=O at 1646 cm^{-1} could be observed [4, 82]. The SBE-β-CD spectrum (b) exhibited characteristic peaks at 3429 and 2934 cm^{-1} related to the O–H and C–H stretching vibrations, respectively. Besides, the H-O-H stretching peak at 1653 cm^{-1}, and a distinctive peak at 1163 cm^{-1} as a consequence of the stretching vibration of C-O-C were noted. Also, the sulfoxide stretching was confirmed by the presence of a strong peak at 1042 cm^{-1} [83, 84]. In the Ph_{CX} spectrum (c), the characteristic absorption peaks of the Hsd at 3476, 1519, 1611, 1276, and 1205 cm^{-1} were maintained. This indicated that Hsd in the Ph_{CX} was not entrapped within the cavity of SBE-β-CD and instead remained uncomplexed. However, sharp peaks of SBE-β-CD dominated in the spectrum of CX (d) with minor shifts of some peaks to lower wave numbers (i.e., 2934 to 2930 cm^{-1}; 1653 to 1639 cm^{-1}) [43, 85]. The peaks of Hsd were not observed in the CX spectrum which could be ascribed to the inclusion within the cavity of SBE-β-CD [86].

DSC

Figure 3B displays the DSC thermograms of Hsd, SBE-β-CD, Ph_{CX}, and CX. Hsd (a) showed an endothermic peak at 105 °C due to the removal of the water of crystallization. A second endothermic peak was observed at 258 °C which could be related to the Hsd melting [87]. In the thermogram of SBE-β-CD (b), a broad endothermic peak was found at 66 °C followed by a sharp endothermic peak at 271 °C. The peaks could be attributed to the dehydration of SBE-β-CD followed by its decomposition. The thermogram of Ph_{CX} exhibited just a collection of the endothermic peaks of Hsd and SBE-β-CD (c). The CX thermogram showed a disappearance of Hsd endothermic peaks with slight broadening and shifting of the sharp SBE-β-CD endothermic peak to 273 °C (d). Thus, the formation of the inclusion complex could be confirmed [79].

XRD

Figure 3C displays the x-ray diffraction patterns of Hsd, SBE-β-CD, Ph_{CX}, and CX. The diffractogram of Hsd (a) displays many characteristic sharp peaks at 12.1, 15.7, 16.5,

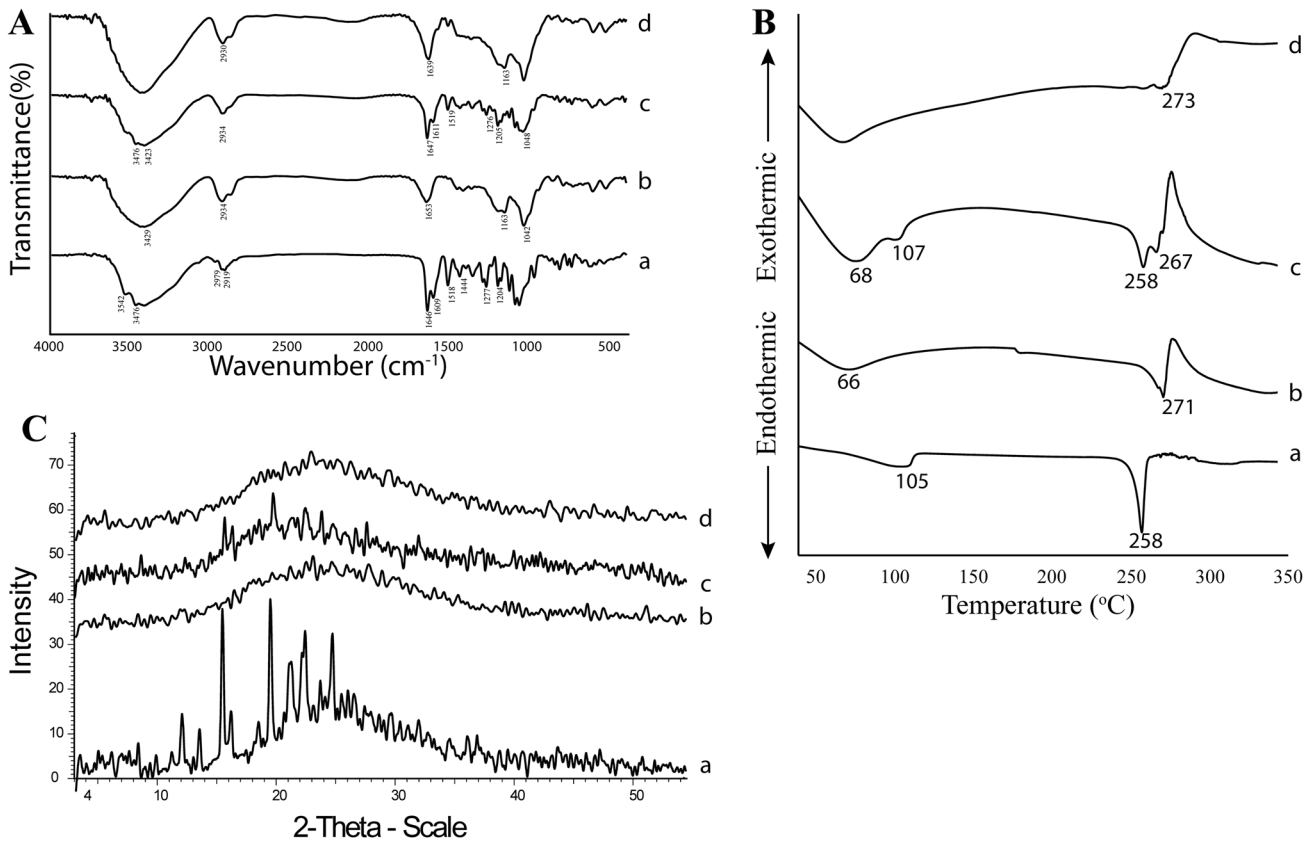

Fig. 3 Solid state characterization of Hsd (a), SBE-β-CD (b), Ph_{CX} (c), and CX (d) using FT-IR (**A**), DSC (**B**), and XRD (**C**). Abbreviations: Hsd, Hesperidin; SBE-β-CD, sulfobutylether-β-cyclodextrin; Ph_{CX}, physical mixture of hesperidin and sulfobutylether-β-cyclodextrin; and CX, hesperidin: sulfobutylether-β-cyclodextrin complex

19.8, 21.6, 22.5, 23.9, and 25° (2θ), which indicated the crystallinity of Hsd [88]. Conversely, the diffractogram of SBE-β-CD (b) exhibited no sharp peaks denoting its amorphous state [89, 90]. The diffraction pattern of Ph_{CX} showed peaks of both Hsd and SBE-β-CD with reduced intensity, revealing a dilution effect due to the presence of two components (c). The diffraction pattern of CX (d) presented an amorphous state with the absence or intensity lessening of the characteristic peaks of Hsd. Such observation deduced the inclusion of Hsd within the cavity of SBE-β-CD associated with diminishing the Hsd crystallinity [91].

^{1}H-NMR

Figure 4 shows the ^{1}H-NMR spectra (DMSO-*d6*) of Hsd and CX. The NMR spectroscopy was conducted to figure out the molar ratio as well as the mode of the interaction between Hsd and SBE-β-CD in the inclusion complex. In the chemical structure of Hsd (Fig. 4A), the B-ring is the phenolic electron richer one due to the contribution of the ortho methoxy group [2]. The formation of CX could be predicted via the inclusion of either the methoxyphenyl moiety or glucopyranosyl unit within the core of the SBE-β-CD molecule. But it was questionable that the hydrophilic glucopyranosyl unit of Hsd was hosted within the lipophilic cavity of SBE-β-CD. However, in our state, due to the coexistence of glucopyranosyl units in Hsd and SBE-β-CD, shifting in H3 and H5 peaks of SBE-β-CD was indistinguishable. Instead, a shifting in ^{1}H-NMR peaks of methoxy (4′-OCH_3) and phenyl protons (2′, 5′, and 6′) of B-ring of Hsd from 3.776 to 3.618 *ppm* and from 6.967 to 6.939 *ppm* was observed, respectively (Fig. 4B). Other peaks of A-ring protons as H6 and H8 remained almost unaltered, ensuring that the inclusion phenomenon of Hsd molecule happened via the modulation of the B-ring into the cavity of SBE-β-CD at molar ratio of 1:1 [92].

SEM

Figure 5 presents the surface morphology of Hsd, SBE-β-CD, Ph_{CX}, and CX. It could be observed that Hsd showed needle-shaped crystals (Fig. 5A) [93, 94]. However, SBE-β-CD exhibited amorphous spherical particles of different sizes (Fig. 5B). The Ph_{CX} morphology demonstrated the

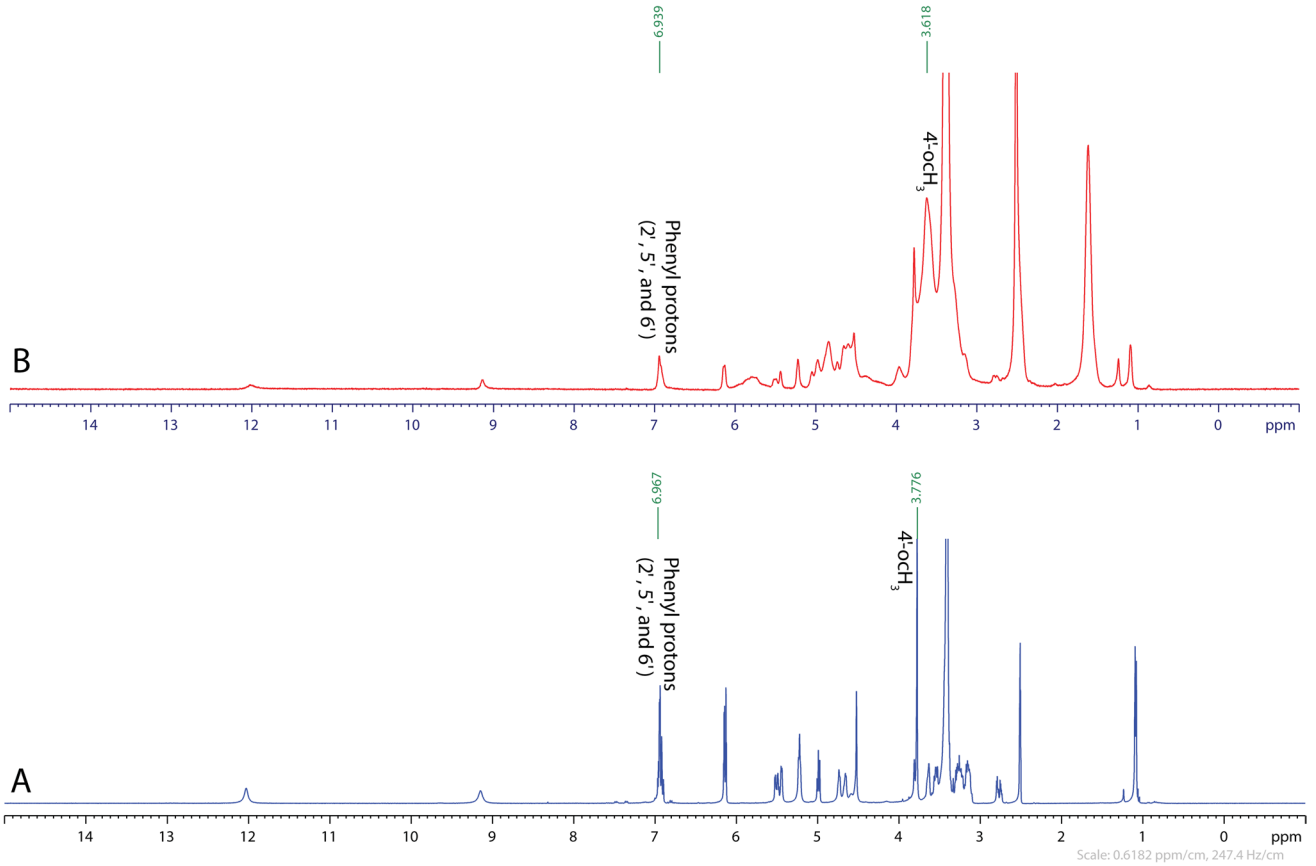

Fig. 4 ^{1}H-NMR spectra of Hsd (**A**) and CX (**B**) in DMSO-*d6*. Abbreviations: Hsd, hesperidin and CX, hesperidin: sulfobutylether-β-cyclodextrin complex

Hsd needle crystals attached to the surface of SBE-β-CD particles while both species preserved their authentic morphology (Fig. 5C). Conversely, the surface morphology of CX (Fig. 5D) displayed erratic particles different from host and guest units, confirming the formation of the inclusion complex [85, 95].

Characterization of Hsd/CD/CS NPs

Entrapment efficiency

The EE% of the prepared Hsd/CD/CS NPs is listed in Table 2. It could be perceived that the EE% of Hsd gradually increased from 14.41 ± 7.00% (F5) to 49.7 ± 3.96% (F2) by increasing the SBE-β-CD equivalent amount of CX from 33.5 to 62.5 mg, respectively. Compared to F2, a significant rise ($P < 0.01$) of the EE% to attain a value of 77.46 ± 0.39% was achieved by augmenting the SBE-β-CD amount to 75 mg (F1). This means that EE% was directly proportional to the amount of CX. Such finding could be attributed to the possible increment of the electrostatic interaction between the negatively charged sulfonyl groups of SBE-β-CD and the protonated amino groups of CS at a high concentration of SBE-β-CD resulting in higher EE% (Table 2) [96].

Particle size, PDI, and ZP

Table 2 documents the particle size, PDI, and ZP of Hsd/CD/CS NPs. The obtained finding confirmed that the prepared NPs were within the nanometric scale (< 1000 nm) and less than 500 nm except for F5 (588.7 ± 5.51 nm). For oral delivery, the particle size < 500 nm favors enterocytic uptake. Moreover, it has been stated that the polymeric NPs of less than 500 nm can traverse the M cells in the intestine, definitely taken up by the lymphatic system, thus overcoming the first pass hepatic metabolism and increasing the bioavailability [97]. The data clarified an eminent decrement in the particle size of NPs ($P < 0.0001$) from 455.7 ± 9.04 nm (F1) to 356.9 ± 12.01 nm (F3) manifested by reducing the SBE-β-CD amount from 75 to 50 mg. This obvious decrease in the particle size of F3 might be related to the corresponding CS:CX ratio (1:1). Such mass ratio might enhance a further electrostatic interaction resulting in a higher degree of

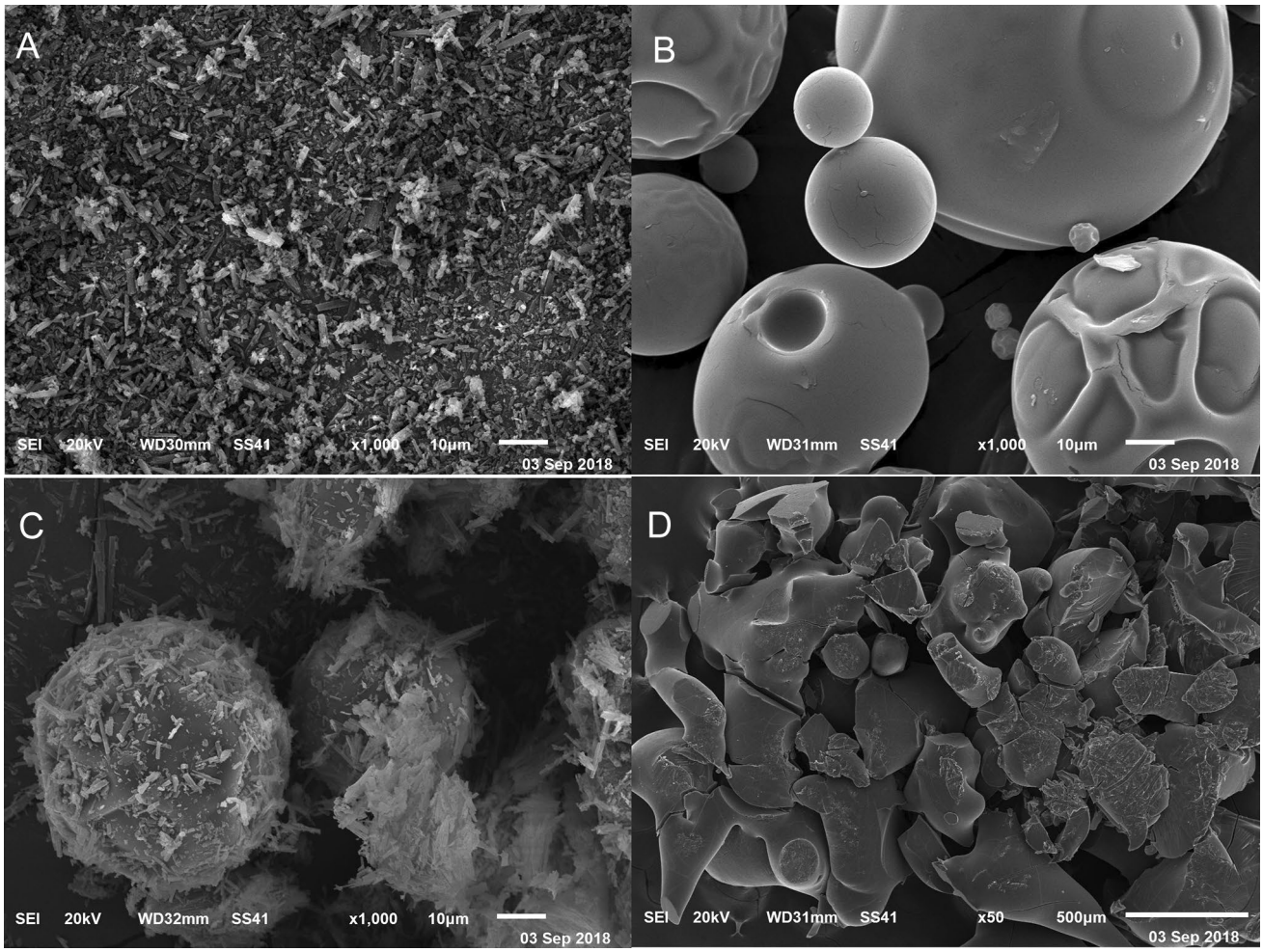

Fig. 5 SEM photomicrographs of Hsd (**A**), SBE-β-CD (**B**), Ph_{CX} (**C**), and CX (**D**). Abbreviations: Hsd, hesperidin; SBE-β-CD, sulfobutylether-β-cyclodextrin; Ph_{CX}, physical mixture of hesperidin and sulfobutylether-β-cyclodextrin; and CX, hesperidin: sulfobutylether-β-cyclodextrin complex

tightness and compaction among the network structure of the Hsd/CD/CS NPs. After that, a further increase of the CS ratio (CS:CX 1:0.67; F5) reflected a significant increment in the particle size up to 588.7 ± 5.51 nm (F5, $P < 0.0001$) [98]. The highest particle size of F5 could be related to the lowest amount of SBE-β-CD as well as the high viscosity of the system. This would lead to a limited inter and intra-molecular crosslinking between CS and CX with a lot of CS molecules remaining unlinked [99]. The excessive positive charge of the free protonated amino groups of the unlinked CS might result in an electrostatic repulsion between the chain of CS followed by swelling, enlargement, and growth of the formed NPs (F5).

Table 2 Characterization of Hsd/CD/CS NPs

Formulation code	Particle size (nm)	PDI	ZP (mV)	EE%	Mucin binding efficiency %
F1	455.7 ± 9.04	0.219 ± 0.01	+32.28 ± 1.12	77.46 ± 0.39	48.70 ± 3.54
F2	440.7 ± 26.77	0.208 ± 0.02	+34.78 ± 4.49	49.70 ± 3.96	54.87 ± 1.86
F3	356.9 ± 12.01	0.208 ± 0.05	+34.40 ± 1.47	32.48 ± 10.04	53.77 ± 8.90
F4	447.4 ± 23.47	0.433 ± 0.12	+35.53 ± 0.57	27.41 ± 4.05	55.27 ± 7.17
F5	588.7 ± 5.51	0.582 ± 0.16	+42.28 ± 3.58	14.41 ± 7.00	58.50 ± 2.70

Each value represents the mean ± SD ($n = 3$)

PDI polydispersity index, *ZP* zeta potential, *EE%* entrapment efficiency percentage

The homogeneity of particle size is expressed as PDI. In our study, the prepared Hsd/Cd/CS NPs displayed a narrow size distribution (PDI values less than 0.5) for F1, F2, F3, and F4 except for F5 (0.582 ± 0.16). It is well known that PDI values less than 0.5 indicate the homogenous nature of the NPs dispersion with narrow size distribution [100–103].

As presented in Table 2, the ZP values of the Hsd/CD/CS NPs from F1 to F4 had a positive surface charge with an amplitude ranging from +32.28 ± 1.12 to +35.53 ± 0.57 mV. After that, F5 with the highest CS:CX ratio (1:0.67) demonstrated an abrupt significant increase of the ZP to reach +42.28 ± 3.58 mV ($P < 0.05$), compared to F4. Typically, the NPs with ZP of more than ±30 mV intend to be considered stable, where they generate efficient repulsive forces to secure better physical colloidal stability, while those with ZP of ±15 mV or less are experienced to be unstable with the possibility of the NPs aggregation [104, 105]. The electrical surface charge of NPs is affected by the particle components and dispersion environment. Moreover, the electrostatic repulsion between NPs significantly affects particle stability, mucoadhesive character, and cellular uptake [106, 107]. The positively charged surface of the Hsd/Cd/CS NPs could be ascribed to the protonated amino groups of CS. The highest ZP value of F5 could be related to the abundance of the protonated amino groups at the higher CS concentration, causing sturdy electrostatic repulsion between NPs. These data are in unison with earlier investigations [108].

Mucoadhesive strength

The mucin-binding efficiencies of the Hsd/Cd/CS NPs are listed in Table 2. It could be observed that the NPs displayed a synchronized increase in the mucin-binding efficiency with the values of ZP. Accordingly, F5 with the highest ZP value of +42.28 ± 3.58 mV possessed the maximum mucin-binding efficiency of 58.50 ± 2.70%. However, other formulations exhibited comparable mucoadhesive activities with values not less than 48.70 ± 3.54% (F1). Simply, the mucoadhesive efficiency could be related to the CS ratio. As the CS amount increased, both the ZP and the mucin-binding efficiency increased. The mucoadhesive nature of CS is related to its cationic character. On the other hand, the acidic sialic and sulfonic moieties of mucin are responsible for its anionic functionalities. The ionic interaction between the cationic groups of CS and anionic acids of the mucin secures the mucoadhesive activity of CS [109, 110]. For oral delivery, this interaction could enhance the gastrointestinal residence time and the enterocyte uptake of the NPs which is crucial for efficient mucosal surrender of therapeutics [111]. Hence, the mucoadhesive property of CS NPs improves both the absorption and the bioavailability of the drug due to prolonged contact with the mucosal layer accompanied by the high surface-to-volume ratio of the NPs [112].

To sum up the above results, F1 presented the maximum EE% of 77.46 ± 0.39%, and particle nano size of 455.7 ± 9.04 nm with narrow distribution (PDI = 0.219 ± 0.01). Moreover, a surface charge of +32.28 ± 1.12 mV resulted in appropriate mucoadhesive strength of 48.70 ± 3.54%. Hence, F1 was subjected to the forthcoming evaluations.

Characterization of the optimal formula (F1)

Transmission electron microscopy (TEM)

Figure 6 shows the TEM micrograph of F1. The TEM affirmed that F1 had aggregate-free spherical-shaped particles. Including the surface and size attributes of NPs, the shape has a magnificent effect on the biological system interaction, enterocytic uptake, and bio-distribution [113]. It had been reported that the spherical-shaped NPs have a higher capacity for cellular internalization in comparison with their rod equivalents. Contrary to the rod NPs, the spherical ones have not extremely affected by the cytoskeleton and are eventually uptaken into cells at a faster rate [114]. Furthermore, the size analysis revealed that the particle size was consistent with that measured by the DLS technique [115, 116].

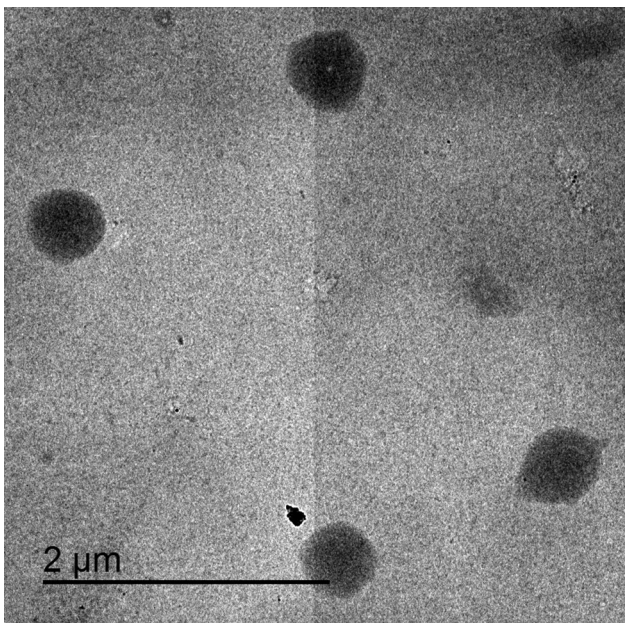

Fig. 6 TEM photomicrograph of F1. Abbreviation: F1, Hsd/CD/CS NPs optimal formula

SEM

Figure 7 illustrates the SEM images of CX, CS, Ph_{NPs}, and F1. The erratic particle morphology of CX was clear (Fig. 7A) [79]. The surface morphology of CS (Fig. 7B) displayed irregular block structures and sometimes elongated sticks [117, 118]. The surface morphology of Ph_{NPs} showed a collection of the individual components (Fig. 7C) [83, 119]. Finally, F1 (Fig. 7D) displayed spherical regular particles embedded within a porous matrix [120, 121].

FT-IR

The FT-IR spectra of F1, and its components as well as PLF1 are presented in Fig. 8A. The CX spectrum (a) was previously discussed under the "FT-IR" section. CS spectrum (b) showed a strong peak at 3448 cm^{-1} assigned to the stretching of the O-H bond and N-H stretching of primary amines as well as the intermolecular H-bonding. A peak at 1076 cm^{-1} and another sharp one at 1424 cm^{-1} could be related to the symmetrical stretching of C-O-C and C-N, respectively. The mode of vibration at 2860 and 2924 cm^{-1} was related to C-H stretching [122]. Also, a strong sharp peak of amide I at 1653 cm^{-1} and amide III at 1320 cm^{-1} were clear. Furthermore, the presence of the CH_2-OH functional group was evident and figured out as a sharp peak at 1380 cm^{-1} [123]. The spectrum of Ph_{NPs} displayed a superposition of the CX and CS spectra (c) [124]. By synchronizing the PLF1 and F1 spectra with those of CS and CX (d and e, respectively), spectral changes were experienced indicating an electrostatic interaction between SBE-β-CD anionic sulfo-butyl groups and CS cationic amine groups. So, the amide I peak shifted from 1653 to 1650 and 1647 cm^{-1} and the amide III peak shifted from 1320 to 1318 and 1323 cm^{-1} for PLF1 and F1, respectively [125]. Also, the peak of amide II appeared at 1543 and 1541 cm^{-1} for PLF1 and F1, respectively [126]. Furthermore, the sulfoxide stretching of 1042 cm^{-1} shifted to 1037 cm^{-1} in both spectra of PLF1 and F1 [127]. Such

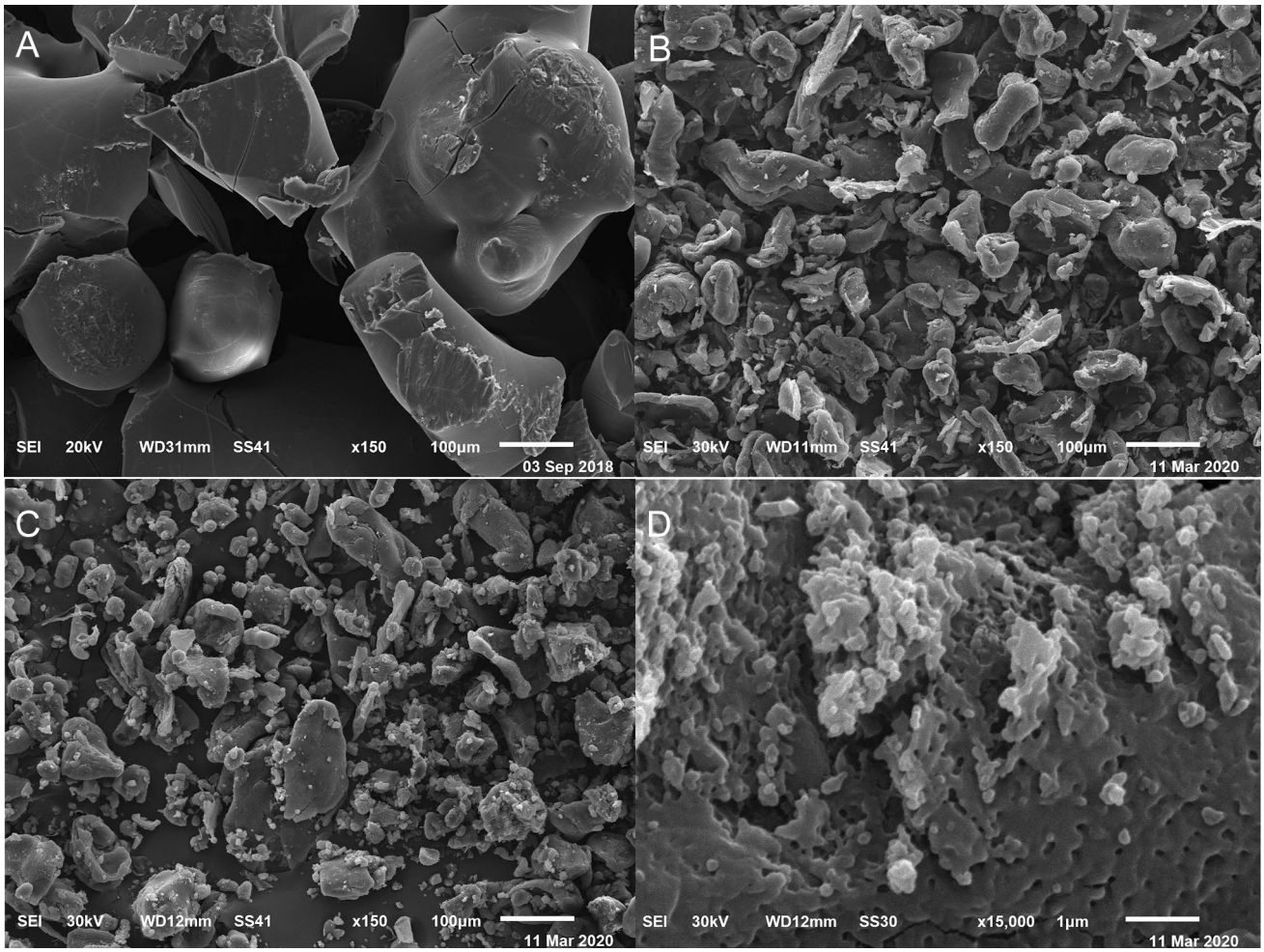

Fig. 7 SEM photomicrographs of CX (**A**), CS (**B**), Ph_{NPs} (**C**), and F1 (**D**). Abbreviations: CX, hesperidin: sulfobutylether-β-cyclodextrin complex; CS, chitosan; Ph_{NPs}, physical mixture of the complex and chitosan; and F1, Hsd/CD/CS NPs optimal formula

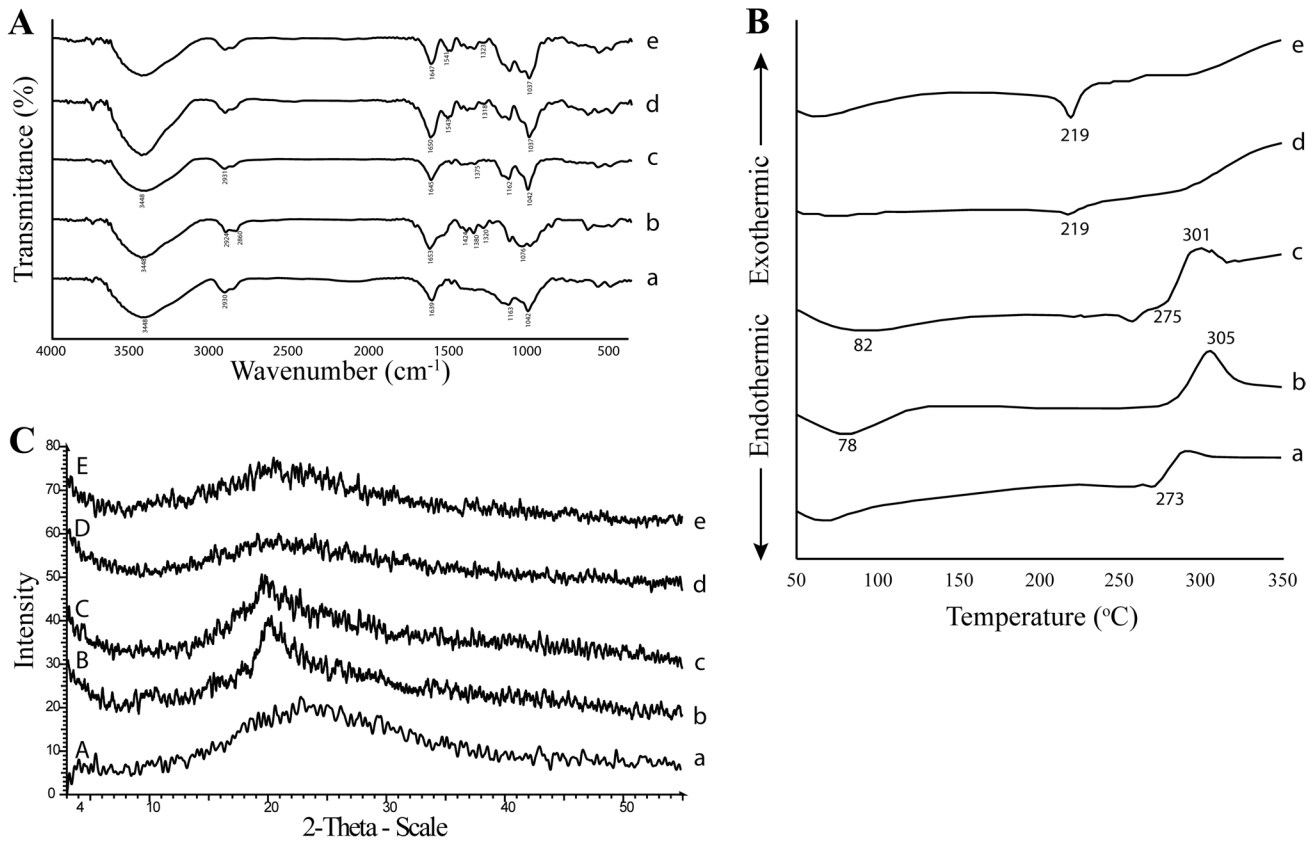

Fig. 8 Solid state characterization of CX (a), CS (b), Ph_{NPs} (c), PLF1 (d), and F1 (e) using FT-IR (**A**), DSC (**B**), and XRD (**C**). Abbreviations: CX, hesperidin: sulfobutylether-β-cyclodextrin complex; CS, chitosan, Ph_{NPs}, physical mixture of the complex and chitosan; PLF1, plain CD/CS NPs optimal formula; and F1, Hsd/CD/CS NPs optimal formula

findings could prove the existence of electrostatic interaction between CS and CX. Subsequently, the formation of the CS NPs could be established.

DSC

Figure 8B depicts the DSC thermograms of CX, CS, Ph_{NPs}, PLF1, and F1. The thermogram of CX (a) was discussed under the "DSC" section, where the endothermal peaks of Hsd disappeared. The CS thermogram (b) showed an endothermic peak at 78 °C referring to the loss of the bound water. Also, another exothermic characteristic peak appeared at 305 °C as a result of the polymer degradation [128, 129]. The Ph_{NPs} thermogram exhibited characteristic peaks of the individual components (c). The PLF1 and F1 thermograms (d and e, respectively) showed that the decomposition peak of SBE-β-CD shifted from 273 to 219 °C confirming the ionic interactions between CS and SBE-β-CD which paved the formation of the NPs [130]. Moreover, the endothermic peak of CS at 78 °C was observed in the range of 60–100 °C indicating that the heat generation during the cross-linking between SBE-β-CD and CS might alter the enthalpy of the NPs [131].

XRD

Figure 8C illustrates the XRD diffractograms of CX, CS, Ph_{NPs}, PLF1, and F1. The diffraction pattern of CX showed its amorphous nature which was previously described under the "XRD" section. (a). Likewise, CS (b) showed one broad characteristic peak at 20° of 2θ indicating its amorphousness [126]. The diffractogram of Ph_{NPs} depicted the overlay of the single components (c) [130]. Broadness was observed in both PLF1 and F1 diffractograms with diminishing peak intensities (d and e, respectively). This could be ascribed to intermolecular hydrogen bonding. Moreover, the complexation of Hsd was responsible for the reduction in its peak intensity which in turn contributes to the amorphousness of the CS NPs [132, 133]. Such observation indicated that the presence of the complexed Hsd did not disturb the nanostructured architecture of the NPs [134].

In vitro release study

The in vitro release patterns of Hsd from CX and F1 in comparison with its diffusion from the aqueous dispersion are illustrated in Fig. 9A–C. Methanolic solutions (40% v/v) at pH 1.2, 6.8, and 7.4 were used as release media to mimic the gastric, intestinal, and physiological environment, respectively. Starting with the gastric pH of 1.2 (Fig. 9A), the free Hsd showed a slow-release pattern to attain only 29.70 ± 2.10% after 12 h. On the other hand, the CX displayed an obvious increase in the release rate of Hsd to reach 90.77 ± 2.25% after 12 h. F1 exhibited an intermediate release percent of 76.77 ± 4.97%. In the intestinal pH of 6.8 (Fig. 9B), the free Hsd and CX offered a percent release of 31.60 ± 2.08 and 93.00 ± 2.12% after 12 h, respectively. While F1 modulated the release of the CX to a slower rate getting 79.90 ± 1.56% within 12 h. At the physiological pH (Fig. 9C), the free Hsd, CX, and F1 exhibited a similar release manner as the above-mentioned ones with a percent of 34.00 ± 1.13, 90.40 ± 1.56, and 75.40 ± 2.69%, respectively. The slowest release rate of the Hsd dispersion could be attributed to its poor aqueous solubility [135–137]. The complexation of Hsd raised the Hsd solubility ("Phase solubility" section) and diminished the Hsd crystallinity as proved under the CX detailed characterization ("Percent complexation and process efficiency", "FT-IR", "DSC", "XRD", "1H-NMR" and "SEM" sections). Hence, CX had a much higher percentage of Hsd release at the studied pH release media [138, 139]. The sustained release of F1 could be referred to that the complexed Hsd had to first depart the

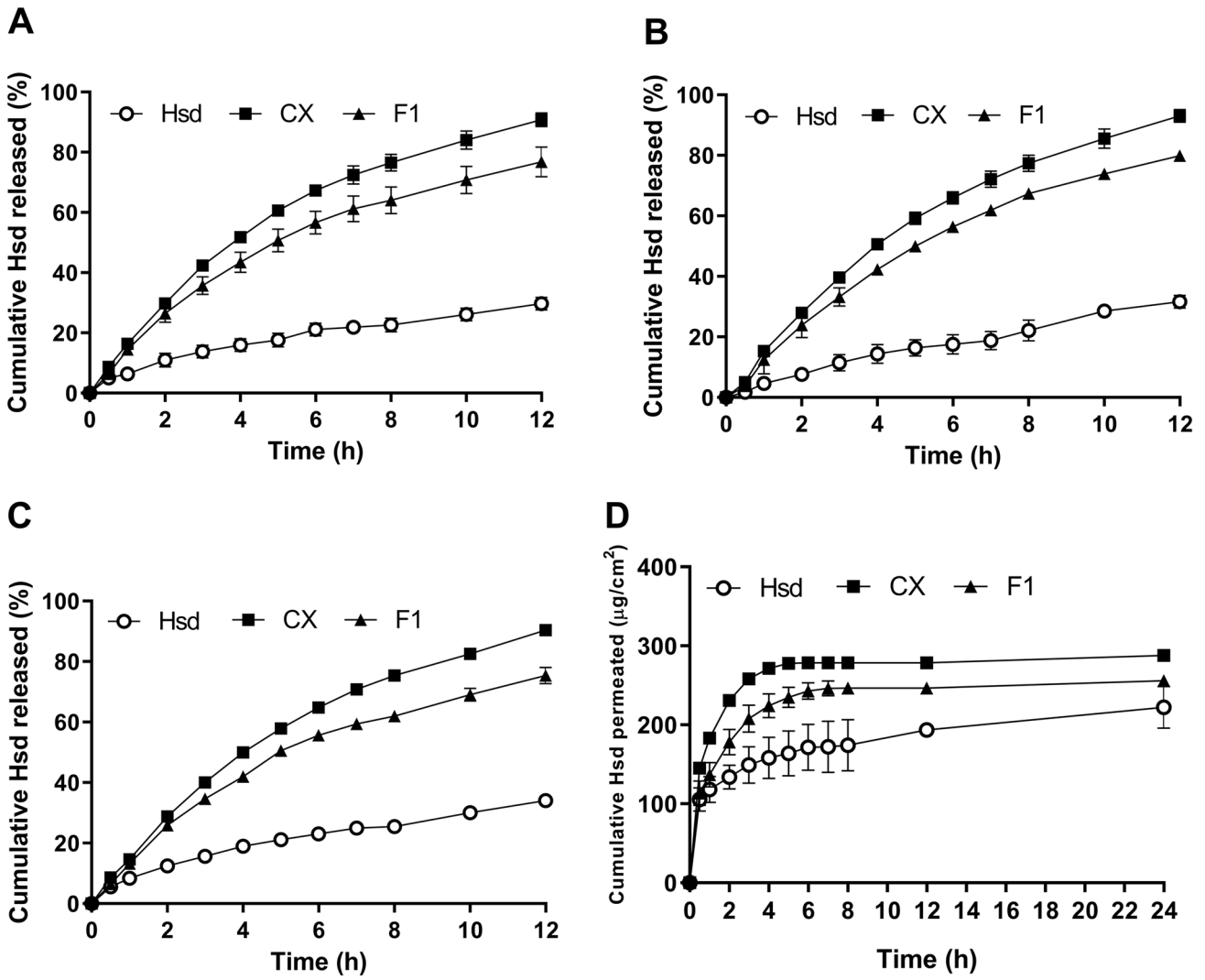

Fig. 9 In vitro release study at pH 1.2 (**A**), 6.8 (**B**), 7.4 (**C**), and the ex vivo intestinal permeation study at pH 7.4 (**D**) of Hsd, CX, and F1. Each point represents the mean ± SD ($n = 3$). Abbreviations: Hsd, hesperidin; CX, hesperidin: sulfobutylether-β-cyclodextrin complex; and F1, Hsd/CD/CS NPs optimal formula

Table 3 Kinetic analysis of the release data of Hsd from aqueous Hsd dispersion, aqueous CX solution, and F1 dispersion at different pH release media

pH release media	Formula	Zero order	First order	Higuchi	Korsmeyer-Peppas		Main transport mechanism
		R^2			R^2	n	
1.2	**Hsd**	0.9394	0.9602	0.994	0.9936	0.5805	Anomalous (non-Fickian) diffusion
	CX	0.9232	0.9962	0.9846	0.9982	0.8498	
	F1	0.923	0.9932	0.9856	0.988	0.8645	
6.8	**Hsd**	0.9817	0.9884	0.9591	0.9846	0.8692	Anomalous (non-Fickian) diffusion
	CX	0.938	0.9845	0.9808	0.9766	1.039	Super case II transport
	F1	0.9423	0.9989	0.9789	0.9733	1.058	
7.4	**Hsd**	0.9373	0.9622	0.9961	0.998	0.5624	Anomalous (non-Fickian) diffusion
	CX	0.9353	0.9933	0.9846	0.9978	0.8485	
	F1	0.9234	0.9907	0.9845	0.9899	0.8429	

Hsd hesperidin, *CX* Hsd/SBE-β-CD complex, *F1* Hsd/CD/CS NPs optimal formula, R^2 coefficient of determination, and *n* diffusion exponent

cavity of SBE-β-CD (complex dissociation) then, cross the network configuration of the CS NPs, and finally diffuse to the release media [140].

Kinetic analysis

Table 3 displays the coefficients of determination of Hsd, CX, and F1 at different pH release media. It could be noted that the Hsd release from its dispersion followed the Higuchi model at both the gastric and the physiological simulating conditions, while the first-order kinetic model fitted its release in the intestinal pH with R^2 values of 0.994, 0.9961, and 0.9884, respectively. The Hsd release from CX and F1 in the gastric, intestinal, and physiological pH was found to follow first-order kinetics with R^2 values exceeding 0.9845 (Table 3). For more exploration of the release kinetics, the Korsmeyer-Peppas equation was employed. The values of *n* are listed in Table 3. It could be noticed that Hsd showed anomalous (non-Fickian) behavior combining both the molecular diffusion and the particle erosion where the n exponents were in the range of 0.5624–0.8692. Also, it was the case for the CX and F1 at pH 1.2 and 7.4. In the intestinal pH (6.8), CX and F1 offered Super case II transport ($n > 0.89$), where the character of dissolution dominated [62].

Ex vivo intestinal permeation

The cumulative Hsd amount permeated (μg/cm^2) across the goat intestine from Hsd dispersion, CX, and F1 is depicted in Fig. 9D. Also, Table 4 displayed the permeation parameters of the studied formulations. The Hsd dispersion showed that an amount of 222.3 ± 26.52 μg/cm^2 of Hsd permeated after 24 h, while CX and F1 depicted cumulative permeated amounts of 287.9 ± 7.29 and 255.6 ± 6.69 μg/cm^2, respectively. The CX depicted a significant increase of J_{ss} (44.95 ± 0.406 μg/cm^2.h) and K_p (0.193 ± 0.002 cm/h) ($P < 0.01$), in comparison to those of Hsd dispersion (20.29 ± 4.657 μg/cm^2.h and 0.087 ± 0.019 cm/h, respectively). The incorporation of CX in F1 demonstrated a significant reduction of the J_{ss} and K_p values to reach 28.13 ± 0.241 μg/cm^2.h and 0.121 ± 0.001 cm/h, respectively ($P < 0.05$). The intestinal permeability of the studied formulation could be arranged as the following: CX > F1 > Hsd. Hsd has been reported to have a weak membrane permeability and consequently, its absorption mainly occurs via the paracellular pathway. This means that the tight junctions of enterocytes might hinder Hsd oral absorption and bioavailability [141, 142]. Due to the poor aqueous solubility of Hsd, increasing its solubility by the complexation could raise its intestinal permeability [143]. Moreover, SBE-β-CD can inhibit P-gp ATPase action, which in sequence increases intestinal permeability [144]. CS is assumed to improve paracellular transport ensuing a structural reorganization of tight junction-associated proteins and then enhancement of intestinal permeation. Moreover, CS is characterized by dedicated mucoadhesive property due to its positive charge which augments the interaction of CS NPs with the intestinal

Table 4 Cumulative permeated amount, flux, and permeability coefficient of Hsd, CX, and F1

Formula	Cumulative permeated amount (μg/cm^2)	J_{ss} (μg/cm^2.h)	K_p (cm/h)
Hsd	222.3 ± 26.52	20.29 ± 4 .657	0.087 ± 0.019
CX	287.9 ± 7.29***	44.95 ± 0.406***	0.193 ± 0.002**
F1	255.6 ± 6.69*	28.13 ± 0.241*	0.121 ± 0.001

Each value represents the mean ± SD ($n = 3$)

Hsd hesperidin, *CX* Hsd/SBE-β-CD complex, *F1* Hsd/CD/CS NPs optimal formula, J_{ss} flux, and K_p permeability coefficient

$^{*}P < 0.05$; $^{**}P < 0.01$; $^{***}P < 0.0001$ versus the corresponding value of Hsd

Table 5 Stability study of F1 at ambient and refrigerated (4 ± 1 °C) temperatures

Parameter		Storage time			
		Zero time	1 month	3 months	6 months
Ambient temperature	**Particle size (nm)**	455.7 ± 9.04	472.3 ± 1.65*	486.9 ± 5.30***	540.9 ± 4.86***
	PDI	0.219 ± 0.005	0.121 ± 0.01***	0.539 ± 0.019***	0.712 ± 0.006***
	ZP (mV)	+32.28 ± 1.12	+30.33 ± 0.38*	+27.39 ± 0.19***	+25.6 ± 0.10***
	DR%	100.00 ± 0.00	95.05 ± 1.38**	92.84 ± 0.88***	90.7 ± 1.30***
Refrigerator temperature (4 ± 1 °C)	**Particle size (nm)**	455.7 ± 9.04	459.1 ± 7.41	460.6 ± 1.04	464.8 ± 2.64^{a}
	PDI	0.219 ± 0.005	0.128 ± 0.015***	0.133 ± 0.003***	0.156 ± 0.003^{a***}
	ZP (mV)	+32.28 ± 1.12	+32.47 ± 1.06	+31.76 ± 0.52	+31.27 ± 0.25^{a}
	DR%	100 ± 0.00	98.88 ± 0.82	98.43 ± 0.43	95.82 ± 1.86^{a**}

Each value represents the mean ± SD ($n = 3$)

PDI polydispersity index, *ZP* zeta potential, *DR%* drug retention percentage, *F1* Hsd/CD/CS NPs optimal formula

$^{*}P < 0.05$; $^{**}P < 0.001$; $^{***}P < 0.0001$ versus the corresponding value at zero time

$^{a}P < 0.0001$ versus the corresponding value at ambient temperature

mucosa [145, 146]. This condition might permit an intimate contact, and extended residence time of F1 to prolong its intestinal permeation [147].

Stability study

Table 5 documents the stability of F1 designated as particle size, PDI, ZP, and DR%. Over the storage period, it was observed that the storage temperatures affected the change rate of the measured parameters. At the ambient temperature, the initial particle size and PDI started to increase significantly during the storage reaching 540.9 ± 4.86 nm and 0.712 ± 0.006, respectively, after 6 months ($P < 0.0001$). Additionally, at the end of the study, the values of ZP and DR% declined significantly to become + 25.60 ± 0.10 mV and 90.70 ± 1.30%, respectively ($P < 0.0001$). Alternatively, the storage of F1 at 4 ± 1 °C for 6 months resulted in a particle size of 464.8 ± 2.64 nm and a ZP of + 31.27 ± 0.25 mV which were not significantly different from those of the corresponding ones at zero time. The values of PDI and DR% did not exceed 0.156 ± 0.003 and 95.82 ± 1.86%, respectively. These data emphasized the superlative stability of F1 at refrigerated temperature, thereby preserving its physicochemical efficacy for long-term storage [70, 145, 148].

Cytotoxicity assay

Figure 10 displays the cell viability of OEC at different concentrations of Hsd, CX, PLF1, and F1 using the WST-1 assay. In literature, Hsd has shown possible cytotoxic activities on several cancer cell lines [149–151]. Consequently, to eliminate the anticancer activity of Hsd, it was necessary

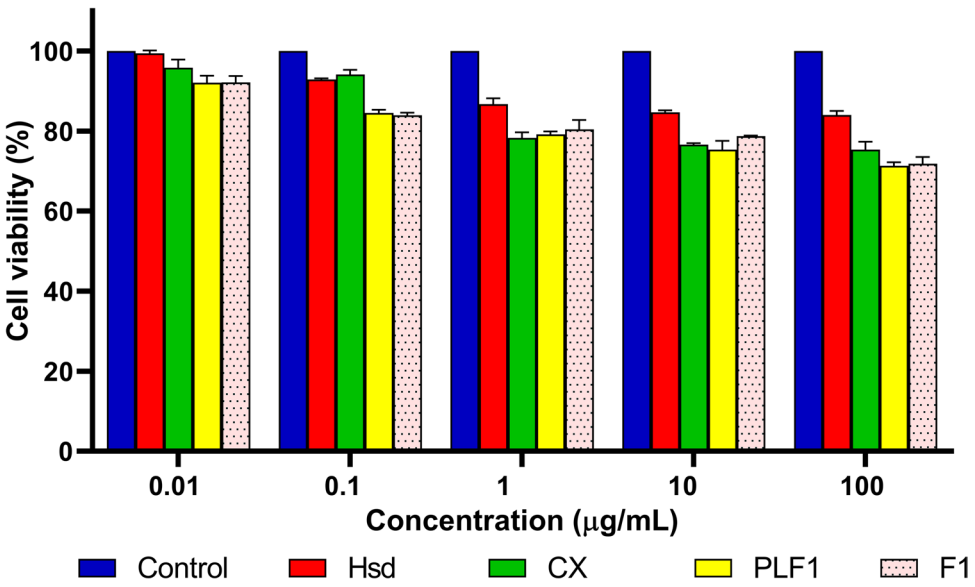

Fig. 10 The percent cell viability of OEC at different concentrations of Hsd, CX, PLF1, and F1. Each point represents the mean ± SD ($n = 3$). Abbreviations: OEC, the normal oral epithelial cell line; Hsd, hesperidin; CX, hesperidin: sulfobutylether-β-cyclodextrin complex; PLF1, Plain CD/CS NPs optimal formula; and F1, Hsd/CD/CS NPs optimal formula

to investigate the cytotoxicity using a normal cell line representing the oral delivery pathway (oral epithelial cell line; OEC). Referring to the results, it could be observed that the studied formulations offered IC_{50} of more than 100 µg/mL assuring their safety on the OEC. Hsd and CX at the concentration of 100 µg/mL showed cell viabilities of 84.00 ± 1.06 and $75.33 \pm 2.01\%$, respectively. Such a decrement ($P < 0.0001$) in the viability by complexation could be ascribed to the improved solubility of the complexed Hsd which in turn might augment more cellular uptake and internalization. Also, PLF1 and F1 at a concentration of 100 µg/mL preserved comparable cell viability values of 71.29 ± 0.89 and $71.86 \pm 1.65\%$, respectively. However, the cell viability > 70% indicated that the tested formulations were well tolerated. The chief components of F1 were SBE-β-CD and CS which exhibited safety and wide applicability in the drug delivery systems. These results agreed with earlier studies that reported the safety of SBE-β-CD even after its complexation with drugs [144, 152–155]. It is well known that CS is an extensively used biocompatible polymer due to its non-toxic and biodegradable nature [156, 157]. Hence, the obtained finding documented the biocompatibility of F1 over the tested concentration range.

In vivo evaluation of the pharmacodynamic hypoglycemic effect

The mean %RBGL after the oral administration of Hsd, CX, and F1 was statistically analyzed, and the resultant data is demonstrated in Fig. 11. Throughout the experiment, Hsd exhibited the lowest hypoglycemic activity compared to CX and F1. After 12 h of the oral administration, Hsd showed a %RBGL of $26.11 \pm 2.66\%$ while CX revealed a significant %RBGL ($P < 0.05$) of $40.60 \pm 2.44\%$. The oral administration of F1 experienced a delayed reduction of the blood glucose level up to 1 h. Then, a faster reduction rate of the blood glucose level was noted to accomplish a significantly higher %RBGL of $61.43 \pm 3.54\%$ ($P < 0.0001$). So, the biological hypoglycemic activity of the investigated formulae can be arranged as the following: F1 > CX > Hsd.

Hyperglycemia may be imputed to reduced hepatic glycogen synthesis together with augmented hepatic glucose production, which may be the reason for reduced glucokinase activities and raised phosphoenolpyruvate carboxykinase and glucose-6-phosphatase activities. The hypoglycemic effect of Hsd could be attributed to the induction of the glucokinase action however declining the phosphoenolpyruvate carboxykinase and glucose-6-phosphatase actions. Moreover, Hsd could ameliorate glucose intolerance and insulin resistance [10, 13]. The solubility of drugs is a key element for their oral absorption. The poor solubility and the minimal permeability of Hsd were early proven and discussed in our study ("Ex vivo intestinal permeation" section). Consequently, the oral administration of Hsd might produce the lowest absorption and the minimal hypoglycemic effect in this study.

Enhancing the solubility of Hsd by complexation with SBE-β-CD improved its dissolution rate and solubility and subsequently could potentiate the oral absorption and pharmacodynamic hypoglycemic effect. Moreover, SBE-β-CD

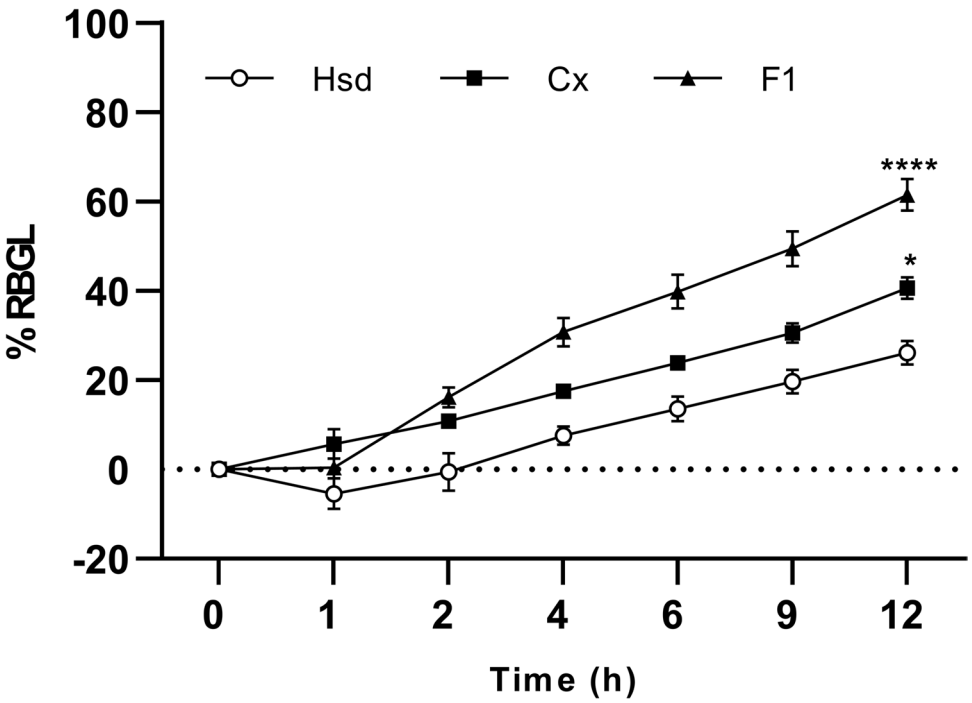

Fig. 11 The hypoglycemic patterns of Hsd, CX, and F1 expressed as %RBGL. Each point represents the mean ± SEM ($n = 3$). Statistical significances of rat groups are indicated as $^{*}P < 0.05$ and $^{****}P < 0.0001$compared to Hsd. Abbreviations: %RBGL, the percent reduction in the blood glucose level; Hsd, hesperidin; CX, hesperidin: sulfobutylether-β-cyclodextrin complex; and F1, Hsd/CD/CS NPs optimal formula

was reported to lessen the viscosity of the intestinal mucus layer and mucosal tissue components (i.e., cholesterol and phospholipids), thereby boosting the permeability at the absorption site [158]. Thus, CX manifested an enhanced hypoglycemic activity over the free Hsd.

It was evident that the hypoglycemic pattern of the orally administered F1 was affected by the physicochemical properties of the CS NPs. The time required for the interaction between the positively charged NPs of F1 (ZP of $+32.28 \pm 1.12$ mV), and the mucosal surface of the gastrointestinal tract might be responsible for this lag time (1 h). Interestingly, studies reported that CS could inhibit hyperglycemia by lessening glucose intestinal digestion, upregulating expression for glucose transporters, and enhancing the cellular uptake of glucose. CS could improve intestinal permeation by its mucoadhesive property and enhanced paracellular pathways [159–161]. Such findings explain the synergistic hypoglycemic effect exerted by F1 that significantly decreased blood glucose levels by the end of the experiment.

Conclusion

In the present study, the solubility of Hsd was significantly enhanced by complexation with SBE-β-CD. Orally nanoparticulate drug delivery systems (Hsd/CD/CS NPs) were successfully prepared by the ionic gelation of CS and SBE-β-CD. Based on a detailed evaluation of the prepared NPs, F1 was the optimal formula possessing the proper particle size, ZP, EE%, and mucoadhesive characteristics. Further examination of F1 revealed transitional release and intestinal permeation compared to Hsd and CX. Also, F1 had not demonstrated any signs of cytotoxicity over the tested concentrations employing normal OEC. The hypoglycemic effect of F1 was found to be worthwhile and considered as a prospective product of unique combined biological activities of the complexed Hsd and CS.

Acknowledgements The authors would like to appreciate Cydex L.C. (USA) for providing us with Captisol®.

Author contribution MEE: methodology, software, validation, data curation, writing—original draft. NMS: conceptualization, visualization, investigation, validation, data curation, supervision, writing—review and editing. IIAH: conceptualization, visualization, investigation, validation, supervision, writing—review and editing.

Funding Open access funding provided by The Science, Technology & Innovation Funding Authority (STDF) in cooperation with The Egyptian Knowledge Bank (EKB).

Availability of data and materials The datasets generated during and/or analyzed during the current study are available from the corresponding author upon reasonable request.

Declarations

Ethical approval The protocol of the study was reviewed and approved by the Ethical Committee of the Faculty of Pharmacy, Mansoura University, Mansoura, Egypt, following the "Principles of Laboratory Animal Care, National Materials Institute of Health Publication (No. 85-23, revised 1985)," (Ethical Approval Code 2023-129).

Informed consent We submit the manuscript entitled: Enhanced oral delivery of hesperidin-loaded sulfobutylether-β-cyclodextrin/chitosan nanoparticles for augmenting its hypoglycemic activity: in vitro-in vivo assessment study. All authors want to have it considered exclusively for publication in "Drug Delivery and Translational Research". We hope our manuscript will have the opportunity to be published in it.

Competing interests The authors declare no competing interests.

References

1. Choi SS, Lee SH, Lee KA. A comparative study of hesperetin, hesperidin and hesperidin glucoside: antioxidant, anti-inflammatory, and antibacterial activities in vitro. Antioxidants. 2022;11:1618.
2. Stanisic D, Liu LHB, dos Santos RV, Costa AF, Durán N, Tasic L. New sustainable process for hesperidin isolation and anti-ageing effects of hesperidin nanocrystals. Molecules. 2020;25:4534.
3. Crescenti A, Caimari A, Alcaide-Hidalgo JM, Mariné-Casadó R, Valls RM, Companys J, et al. Hesperidin bioavailability is increased by the presence of 2S-diastereoisomer and micronization—a randomized, crossover and double-blind clinical trial. Nutrients. 2022;14:2481.
4. Rekha SS, Pradeepkiran JA, Bhaskar M. Bioflavonoid hesperidin possesses the anti-hyperglycemic and hypolipidemic property in STZ induced diabetic myocardial infarction (DMI) in male Wister rats. J Nutr Intermed Metab. 2019;15:58–64.
5. Chimagave SS, Jalalpure SS, Patil AK, Kurangi BK. Development and validation of stability indicating UV-spectrophotometric method for the estimation of hesperidin in bulk drugs, plant extract, Ayurveda formulation and nanoformulation. Indian J Pharm Educ Res. 2022;56:865–72.
6. Dangre PV, Tattu AD, Borikar SP, Surana SJ, Chalikwar SS. Development and statistical optimization of alginate-Neusilin US2 micro-composite beads to elicit gastric stability and sustained action of hesperidin. Int J Biol Macromol. 2021;171:514–26.
7. Saad S, Ahmad I, Kawish SM, Khan UA, Ahmad FJ, Ali A, et al. Improved cardioprotective effects of hesperidin solid lipid nanoparticles prepared by supercritical antisolvent technology. Colloids Surf B Biointerfaces. 2020;187:110628.

8. Truzzi E, Benvenuti S, Bertelli D, Scozzoli M. Optimization and validation of a high-performance liquid chromatography method for the analysis of hesperidin and carvacrol for veterinary use. Am J Anal Chem. 2021;12:459–70.
9. Homayouni F, Haidari F, Hedayati M, Zakerkish M, Ahmadi K. Hesperidin supplementation aleviates oxidative DNA damage and lipid peroxidation in type 2 diabetes: a randomized double-blind placebo-controlled clinical trial. Phytother Res. 2017;31:1539–45.
10. Peng P, Jin J, Zou G, Sui Y, Han Y, Zhao D, et al. Hesperidin prevents hyperglycemia in diabetic rats by activating the insulin receptor pathway. Exp Ther Med. 2020;21:53.
11. Shehata AS, Mohamed DA, Hagras SM, El-Beah SM, Elnegris HM. The role of hesperidin in ameliorating retinal changes in rats with experimentally induced type 1 diabetes mellitus and the active role of vascular endothelial growth factor and glial fibrillary acidic protein. Anat Cell Biol. 2021;54:465–78.
12. Chen YJ, Kong L, Tang ZZ, Zhang YM, Liu Y, Wang TY, et al. Hesperetin ameliorates diabetic nephropathy in rats by activating Nrf2/ARE/glyoxalase 1 pathway. Biomed Pharmacother. 2019;111:1166–75.
13. Syed AA, Reza MI, Yadav H, Gayen JR. Hesperidin inhibits NOX4 mediated oxidative stress and inflammation by upregulating SIRT1 in experimental diabetic neuropathy. Exp Gerontol. 2023;172:112064.
14. Morsy MA, Nair AB. Prevention of rat liver fibrosis by selective targeting of hepatic stellate cells using hesperidin carriers. Int J Pharm. 2018;552:241–50.
15. Sip S, Sip A, Miklaszewski A, Żarowski M, Cielecka-Piontek J. Zein as an effective carrier for hesperidin delivery systems with improved prebiotic potential. Molecules. 2023;28:5209.
16. Ho S, Thoo YY, Young DJ, Siow LF. Stability and recovery of cyclodextrin encapsulated catechin in various food matrices. Food Chem. 2019;275:594–9.
17. Lai WF, Rogach AL, Wong WT. Chemistry and engineering of cyclodextrins for molecular imaging. Chem Soc Rev. 2017;46:6379–419.
18. Lu J, Li X, Qiu C, McClements DJ, Jiao A, Wang J, et al. Preparation and characterization of food-grade pickering emulsions stabilized with chitosan-phytic acid-cyclodextrin nanoparticles. Foods. 2022;11:450.
19. Osborne IJ, Mace S, Taylor D. A prospective year-long follow-up of lurasidone use in clinical practice: factors predicting treatment persistence. Ther Adv Psychopharmacol. 2018;8:117–25.
20. Rinaki E, Dokoumetzidis A, Macheras P. The mean dissolution time depends on the dose/solubility ratio. Pharm Res. 2003;20:406–8.
21. Szejtli J. Introduction and general overview of cyclodextrin chemistry. Chem Rev. 1998;98:1743–54.
22. Kulkarni AD, Belgamwar VS. Inclusion complex of chrysin with sulfobutyl ether-β-cyclodextrin (Captisol®): preparation, characterization, molecular modelling and in vitro anticancer activity. J Mol Struct. 2017;1128:563–71.
23. Shen M, Wu M, Tan X, Song Z. Study on the inclusion interaction between sulfobutylether-β-cyclodextrin and clozapine by flow injection chemiluminescence. Instrum Sci Technol. 2014;42:46–58.
24. Wang, Zhang. Comment about the safety of intravenous voriconazole formulated with sulfobutylether beta-cyclodextrin. J Mol Struct. 2022;1128:563–71.
25. Kaczmarek-Szczepańska B, Sionkowska MM, Mazur O, Świątczak J, Brzezinska MS. The role of microorganisms in biodegradation of chitosan/tannic acid materials. Int J Biol Macromol. 2021;184:584–92.
26. Ebru UZ, Balabanli B, Cevher ŞC. Vascular endothelial growth factor supplementation enhance skin antioxidant capacity in hyperglycemic rats. Gazi Univ J Sci. 2022;1–1.
27. Wu CS, Hsu YC, Liao HT, Cai YX. Antibacterial activity and in vitro evaluation of the biocompatibility of chitosan-based polysaccharide/polyester membranes. Carbohydr Polym. 2015;134:438–47.
28. Bakshi PS, Selvakumar D, Kadirvelu K, Kumar NS. Chitosan as an environment friendly biomaterial – a review on recent modifications and applications. Int J Biol Macromol. 2020;150:1072–83.
29. Ngo DH, Vo TS, Ngo DN, Kang KH, Je JY, Pham HND, et al. Biological effects of chitosan and its derivatives. Food Hydrocoll. 2015;51:200–16.
30. Abruzzo A, Zuccheri G, Belluti F, Provenzano S, Verardi L, Bigucci F, et al. Chitosan nanoparticles for lipophilic anticancer drug delivery: development, characterization and in vitro studies on HT29 cancer cells. Colloids Surf B Biointerfaces. 2016;145:362–72.
31. Desai KG. Chitosan nanoparticles prepared by ionotropic gelation: an overview of recent advances. Crit Rev Ther Drug Carrier Syst. 2016;33:107–58.
32. Ahmad W, Quazi J. Formulation and evaluation as sustain released nanoparticles for zolmitriptan hydrochloride for the enhanced bioavailability and better therapeutic action by using chitosan as a permeation enhancer. Res J Pharm Dos Forms Technol. 2023;85–90.
33. Zhang J, Xia W, Liu P, Cheng Q, Tahi T, Gu W, et al. Chitosan modification and pharmaceutical/biomedical applications. Mar Drugs. 2010;8:1962–87.
34. Calderón L, Harris R, Cordoba-Diaz M, Elorza M, Elorza B, Lenoir J, et al. Nano and microparticulate chitosan-based systems for antiviral topical delivery. Eur J Pharm Sci. 2013;48:216–22.
35. Priyanka DN, Prashanth KVH, Tharanathan RN. A review on potential anti-diabetic mechanisms of chitosan and its derivatives. Carbohydr Polym Technol Appl. 2022;3:100188.
36. Perumal V, Manickam T, Bang KS, Velmurugan P, Oh BT. Antidiabetic potential of bioactive molecules coated chitosan nanoparticles in experimental rats. Int J Biol Macromol. 2016;92:63–9.
37. El-Shahawy AAG, Abdel-Moneim A, Ebeid ASM, Eldin ZE, Zanaty MI. A novel layered double hydroxide-hesperidin nanoparticles exert antidiabetic, antioxidant and anti-inflammatory effects in rats with diabetes. Mol Biol Rep. 2021;48:5217–32.
38. Gaur PK, Pal H, Puri D, Kumar N, Shanmugam SK. Formulation and development of hesperidin loaded solid lipid nanoparticles for diabetes. Biointerface Res Appl Chem. 2019;10:4728–33.
39. Satheesh Kumar D, Shailendra Kumar, Ravichandran S. In vivo antidiabetic evaluation of nanoparticles encompass dual bioflavonoid. Int J Pharmacomet Integr Biosci. 2018;3:11–8.
40. Das SK, Chakraborty S, Bose A, Rajabalaya R, Khanam J. Effects of the preparation technique on the physicochemical characteristics and dissolution improvement of ketoprofen-SBE7-β-CD binary inclusion complexes. Colloids Surf Physicochem Eng Asp. 2021;611:125775.
41. Yang J, Ma Y, Luo Q, Liang Z, Lu P, Song F, et al. Improving the solubility of vorinostat using cyclodextrin inclusion complexes: the physicochemical characteristics, corneal permeability and ocular pharmacokinetics of the drug after topical application. Eur J Pharm Sci. 2022;168:106078.
42. Zhang Y, Zhao Z, Wang K, Lyu K, Yao C, Li L, et al. Molecular docking assisted exploration on solubilization of poorly soluble drug remdesivir in sulfobutyl ether-tycyclodextrin. AAPS Open. 2022;8:9.
43. Cutrignelli A, Lopedota A, Denora N, Iacobazzi RM, Fanizza E, Laquintana V, et al. A new complex of curcumin with sulfobutylether-β-cyclodextrin: characterization studies and

in vitro evaluation of cytotoxic and antioxidant activity on HepG-2 cells. J Pharm Sci. 2014;103:3932–40.
44. de Oliveira Nonato R, Krawczk-Santos AP, Cardoso G, Kogawa AC, Ricommini K, Lima AAN, et al. Cyclodextrin inclusion complex of a multi-component natural product by hot-melt extrusion [Internet]. In Review. 2022. Available from: https://www.researchsquare.com/article/rs-1745699/v1.
45. Ramesh KV. Characterization of sulfobutyl ether beta-cyclodextrin binary and ternary inclusion complexes of loratadine. Asian J Pharm. 2020;14.
46. Novac M, Musuc AM, Ozon EA, Sarbu I, Mitu MA, Rusu A, et al. Manufacturing and assessing the new orally disintegrating tablets, containing nimodipine-hydroxypropyl-β-cyclodextrin and nimodipine-methyl-β-cyclodextrin inclusion complexes. Molecules. 2022;27:2012.
47. Wu J, Shen Q, Fang L. Sulfobutylether-β-cyclodextrin/chitosan nanoparticles enhance the oral permeability and bioavailability of docetaxel. Drug Dev Ind Pharm. 2013;39:1010–9.
48. Liu B, Zhu X, Zeng J, Zhao J. Preparation and physicochemical characterization of the supramolecular inclusion complex of naringin dihydrochalcone and hydroxypropyl-β-cyclodextrin. Food Res Int. 2013;54:691–6.
49. Luo X, Zeng L, Li Q, Wang Z, Kong F, Bi Y. β-cyclodextrin inclusion complex containing essential oil from wampee [Clausena lansium (Lour.) Skeels] fruit pericarp: synthesis, characterization, and evaluation of antioxidant activity. J Mol Struct. 2022;1266:133525.
50. Abruzzo A, Croatti V, Zuccheri G, Pasquale Nicoletta F, Sallustio V, Corazza E, et al. Drug-in-cyclodextrin-in-polymeric nanoparticles: a promising strategy for rifampicin administration. Eur J Pharm Biopharm. 2022;180:190–200.
51. Mahmoud AA, El-Feky GS, Kamel R, Awad GEA. Chitosan/sulfobutylether-β-cyclodextrin nanoparticles as a potential approach for ocular drug delivery. Int J Pharm. 2011;413:229–36.
52. Fülöp Z, Saokham P, Loftsson T. Sulfobutylether-β-cyclodextrin/chitosan nano- and microparticles and their physicochemical characteristics. Int J Pharm. 2014;472:282–7.
53. Wang Z, Li Y. Raloxifene/SBE-β-CD inclusion complexes formulated into nanoparticles with chitosan to overcome the absorption barrier for bioavailability enhancement. Pharmaceutics. 2018;10:76.
54. Erdoğar N, Akkın S, Nielsen TT, Özçelebi E, Erdoğdu B, Nemutlu E, et al. Development of oral aprepitant-loaded chitosan–polyethylene glycol-coated cyclodextrin nanocapsules: formulation, characterization, and pharmacokinetic evaluation. J Pharm Investig. 2021;51:297–310.
55. He M, Zhong C, Hu H, Jin Y, Chen Y, Lou K, et al. Cyclodextrin/chitosan nanoparticles for oral ovalbumin delivery: preparation, characterization and intestinal mucosal immunity in mice. Asian J Pharm Sci. 2019;14:193–203.
56. Dyawanapelly S, Koli U, Dharamdasani V, Jain R, Dandekar P. Improved mucoadhesion and cell uptake of chitosan and chitosan oligosaccharide surface-modified polymer nanoparticles for mucosal delivery of proteins. Drug Deliv Transl Res. 2016;6:365–79.
57. Fathima E, Nallamuthu I, Anand T, Naika M, Khanum F. Enhanced cellular uptake, transport and oral bioavailability of optimized folic acid-loaded chitosan nanoparticles. Int J Biol Macromol. 2022;208:596–610.
58. Tzeyung A, Md S, Bhattamisra S, Madheswaran T, Alhakamy N, Aldawsari H, et al. Fabrication, optimization, and evaluation of rotigotine-loaded chitosan nanoparticles for nose-to-brain delivery. Pharmaceutics. 2019;11:26.
59. Durán N, Costa AF, Stanisic D, Bernardes JS, Tasic L. Nanotoxicity and dermal application of nanostructured lipid carrier loaded with hesperidin from orange residue. J Phys Conf Ser. 2019;1323: 012021.
60. Higuchi T. Mechanism of sustained- action medication theoretical analysis of rate of release of solid drugs dispersed in solid matrices. J Pharmaceirtical Sci. 1963;52:1145–90.
61. Korsmeyer RW, Gurny R, Doelker E, Buri P, Peppas NA. Mechanisms of solute release from porous hydrophilic polymers. Int J Pharm. 1983;15:25–35.
62. Abdel Raheem IA, Abdul Razek A, Elgendy AA, Saleh NM, Shaaban MI, Abd El-Hady FK. Design, evaluation and antimicrobial activity of Egyptian propolis-loaded nanoparticles: intrinsic role as a novel and naturally based root canal nanosealer. Int J Nanomed. 2019;14:8379–98.
63. Fouladian P, Afinjuomo F, Arafat M, Bergamin A, Song Y, Blencowe A, et al. Influence of polymer composition on the controlled release of docetaxel: a comparison of non-degradable polymer films for oesophageal drug-eluting stents. Pharmaceutics. 2020;12:444.
64. Bapat P, Ghadi R, Chaudhari D, Katiyar SS, Jain S. Tocophersolan stabilized lipid nanocapsules with high drug loading to improve the permeability and oral bioavailability of curcumin. Int J Pharm. 2019;560:219–27.
65. Kaur I, Nallamothu B, Kuche K, Katiyar SS, Chaudhari D, Jain S. Exploring protein stabilized multiple emulsion with permeation enhancer for oral delivery of insulin. Int J Biol Macromol. 2021;167:491–501.
66. Khalifa AZM, Abdul Rasool BK. Optimized mucoadhesive coated niosomes as a sustained oral delivery system of famotidine. AAPS PharmSciTech. 2017;18:3064–75.
67. Gungor Ak A, Turan I, Sayan Ozacmak H, Karatas A. Chitosan nanoparticles as promising tool for berberine delivery: formulation, characterization and in vivo evaluation. J Drug Deliv Sci Technol. 2023;80:104203.
68. Jalal RR, Ways TMM, Abu Elella MH, Hassan DA, Khutoryanskiy VV. Preparation of mucoadhesive methacrylated chitosan nanoparticles for delivery of ciprofloxacin. Int J Biol Macromol. 2023;242:124980.
69. Romić MD, Sušac A, Lovrić J, Cetina-Čižmek B, Filipović-Grčić J, Hafner A. Evaluation of stability and *in vitro* wound healing potential of melatonin loaded (lipid enriched) chitosan based microspheres. Acta Pharm. 2019;69:635–48.
70. Pandey P, Dua K, Dureja H. Erlotinib loaded chitosan nanoparticles: formulation, physicochemical characterization and cytotoxic potential. Int J Biol Macromol. 2019;139:1304–16.
71. Hazekawa M, Nishinakagawa T, Kawakubo-Yasukochi T, Nakashima M. Evaluation of IC50 levels immediately after treatment with anticancer reagents using a real-time cell monitoring device. Exp Ther Med [Internet]. 2019 [cited 2023 Jul 21]; Available from: http://www.spandidos-publications.com/10.3892/etm.2019.7876.
72. Tajodini M, Samadi F, Asadi J, Khosravi A, Samadi F. Anticancer and apoptotic effects of orange peel extract and naringin on doxorubicin-induced apoptosis in human esophageal squamous carcinoma cell line [Internet]. In Review. 2023. Available from: https://www.researchsquare.com/article/rs-3068410/v1.
73. Abu Hashim II, Higashi T, Anno T, Motoyama K, Abd-ElGawad AEH, El-Shabouri MH, et al. Potential use of γ-cyclodextrin polypseudorotaxane hydrogels as an injectable sustained release system for insulin. Int J Pharm. 2010;392:83–91.
74. Deng W, Wang H, Wu B, Zhang X. Selenium-layered nanoparticles serving for oral delivery of phytomedicines with hypoglycemic activity to synergistically potentiate the antidiabetic effect. Acta Pharm Sin B. 2019;9:74–86.
75. Awadeen RH, Boughdady MF, Meshali MM. New *in-situ* gelling biopolymer-based matrix for bioavailability enhancement of glimepiride; *in-vitro* / *in-vivo* x-ray imaging and pharmacodynamic evaluations. Pharm Dev Technol. 2019;24:539–49.

76. Mohamed EA, Meshali MM, Foda AMM, Borg TM. Improvement of dissolution and hypoglycemic efficacy of glimepiride by different carriers. AAPS PharmSciTech. 2012;13:1013–23.
77. Chaudhari P, Naik R, Sruthi Mallela L, Roy S, Birangal S, Ghate V, et al. A supramolecular thermosensitive gel of ketoconazole for ocular applications: in silico, in vitro, and ex vivo studies. Int J Pharm. 2022;613:121409.
78. Higuchi, Conors. Phase solubility techniques. Phase-Solubility Tech Adv Anal Chem Instrum. 1965;4:117–212.
79. Xu J, Zhang Y, Li X, Zheng Y. Inclusion complex of nateglinide with sulfobutyl ether β-cyclodextrin: preparation, characterization and water solubility. J Mol Struct. 2017;1141:328–34.
80. Martins LNSB, Venceslau AFA, Brandão RM, Braga MA, Batista LR, Cardoso M das G, et al. Antibacterial and antifungal activities and toxicity of the essential oil from Callistemon viminalis complexed with β-cyclodextrin. Curr Microbiol. 2021;78:2251–8.
81. Wen P, Zhu DH, Feng K, Liu FJ, Lou WY, Li N, et al. Fabrication of electrospun polylactic acid nanofilm incorporating cinnamon essential oil/ β -cyclodextrin inclusion complex for antimicrobial packaging. Food Chem. 2016;196:996–1004.
82. Lahmer N, Belboukhari N, Cheriti A, Sekkoum K. Hesperidin and hesperitin preparation and purification from Citrus sinensis peels. Pharma Chem. 2015;7:1–4.
83. Alvi Z, Akhtar M, Mahmood A, Ur-Rahman N, Nazir I, Sadaquat H, et al. Enhanced oral bioavailability of epalrestat SBE7-β-CD complex loaded chitosan nanoparticles: preparation, characterization and in-vivo pharmacokinetic evaluation. Int J Nanomed. 2021;16:8353–73.
84. Soe HMSH, Kerdpol K, Rungrotmongkol T, Pruksakorn P, Autthateinchai R, Wet-osot S, et al. Voriconazole eye drops: enhanced solubility and stability through ternary voriconazole/sulfobutyl ether β-cyclodextrin/polyvinyl alcohol complexes. Int J Mol Sci. 2023;24:2343.
85. Kong F, Su Z, Zhang L, Qin Y, Zhang K. Inclusion complex of grape seeds extracts with sulfobutyl ether β-cyclodextrin: preparation, characterization, stability and evaluation of α-glucosidase and α-amylase inhibitory effects in vitro. LWT. 2019;101:819–26.
86. Bhadale R, Londhe V. Inclusion complex of iloperidone with sulfobutyl ether beta-cyclodextrin: characterization and dissolution studies. 1st Int Electron Conf Pharm [Internet]. MDPI; 2020 [cited 2023 Feb 19]. p. 22. Available from: https://www.mdpi.com/2504-3900/78/1/22.
87. Gao H, Chen Y, Ma H, Zeng J, Li G. Preparation and characterization of hesperidin - PEG 6000 complex. J Chem Soc Pak. 2014;36:848–51.
88. Varghese JJ, Mallya R. Formulation development and evaluation of antioxidant potential of hesperidin nanocrystals. World J Pharm Res. 2015;4:23.
89. Soe HM, Chamni S, Mahalapbutr P, Kongtaworn N, Rungrotmongkol T, Jansook P. The investigation of binary and ternary sulfobutylether-β-cyclodextrin inclusion complexes with asiaticoside in solution and in solid state. Carbohydr Res. 2020;498:108190.
90. Yue L, Jin W, Chi S, Yang T, Lei Z, Zhu H, et al. pH-RESPONSIVE chitosan/sulfobutyl ether-β-cyclodextrin supramolecular nanoparticles for controlled release of sodium ferulate. Polym Eng Sci. 2020;60:2403–13.
91. Maqbool I, Akhtar M, Ahmad R, Sadaquat H, Noreen S, Batool A, et al. Novel multiparticulate pH triggered delayed release chronotherapeutic drug delivery of celecoxib-β-cyclodextrin inclusion complexes by using Box-Behnken design. Eur J Pharm Sci. 2020;146:105254.
92. Corciova A, Ciobanu C, Poiata A, Mircea C, Nicolescu A, Drobota M, et al. Antibacterial and antioxidant properties of hesperidin: β-cyclodextrin complexes obtained by different techniques. J Incl Phenom Macrocycl Chem. 2015;81:71–84.
93. Inoue T, Yoshinaga A, Takabe K, Yoshioka T, Ogawa K, Sakamoto M, et al. *In situ* detection and identification of hesperidin crystals in satsuma mandarin (*Citrus unshiu*) peel cells: *in situ* detection of hesperidin crystals in *citrus* peel cells. Phytochem Anal. 2015;26:105–10.
94. Rebouças LM, Sousa ACC, Sampaio CG, Silva LMR, Costa PMS, Pessoa C, et al. Microcapsules based on alginate and guar gum for co-delivery of hydrophobic antitumor bioactives. Carbohydr Polym. 2023;301:120310.
95. Wang J, Huang B, Dai J, Chen G, Ren L. Inclusion complex of lurasidone hydrochloride with Sulfobutylether-β-cyclodextrin has enhanced oral bioavailability and no food effect. Am J Transl Res. 2022;14:1495–506.
96. Csaba N, Köping-Höggård M, Alonso MJ. Ionically crosslinked chitosan/tripolyphosphate nanoparticles for oligonucleotide and plasmid DNA delivery. Int J Pharm. 2009;382:205–14.
97. Gheybi E, Asoodeh A, Amani J. Preparation of chitosan nanoparticle containing recombinant CD44v antigen and evaluation of its immunization capacity against breast cancer in BALB/c mice. BMC Cancer. 2023;23:134.
98. Liu F, Antoniou J, Li Y, Majeed H, Liang R, Ma Y, et al. Chitosan/sulfobutylether-β-cyclodextrin nanoparticles as a potential approach for tea polyphenol encapsulation. Food Hydrocoll. 2016;57:291–300.
99. Bin-Jumah M, Gilani SJ, Jahangir MA, Zafar A, Alshehri S, Yasir M, et al. Clarithromycin-loaded ocular chitosan nanoparticle: formulation, optimization, characterization, ocular irritation, and antimicrobial activity. Int J Nanomedicine. 2020;15:7861–75.
100. Abd ElRahman N, Marzouk M, Elbakry A, Elhosary R. Polymeric nanoparticles based transdermal hydrogel of terbutaline sulphate: formulation and evaluation. Azhar Int J Pharm Med Sci. 2023;0:0–0.
101. Md S, Khan RA, Mustafa G, Chuttani K, Baboota S, Sahni JK, et al. Bromocriptine loaded chitosan nanoparticles intended for direct nose to brain delivery: pharmacodynamic, pharmacokinetic and scintigraphy study in mice model. Eur J Pharm Sci. 2013;48:393–405.
102. Rosyada A, Sunarharum WB, Waziiroh E. Characterization of chitosan nanoparticles as an edible coating material. In: IOP Conf Ser Earth Environ Sci. 2019. p. 230:012043.
103. Venegas-García DJ, Wilson LD. Kinetics and thermodynamics of adsorption for aromatic hydrocarbon model systems via a coagulation process with a ferric sulfate–lime softening system. Materials. 2023;16:655.
104. Lashari N, Ganat T, Elraies KA, Ayoub MA, Kalam S, Chandio TA, et al. Impact of nanoparticles stability on rheology, interfacial tension, and wettability in chemical enhanced oil recovery: a critical parametric review. J Pet Sci Eng. 2022;212:110199.
105. Taheri M, Maaref S, Kantzas A, Bryant S, Trudel S. Improving the colloidal stability of PEGylated BaTiO3 nanoparticles with surfactants. Chem Phys. 2023;564:111701.
106. Abeer Ramadan Mohamed AEA, Monira Rashed AO, Mahmoud MA, Shehata SM, Abdelazim NS. Chitosan nanoparticles as a carrier for *Mentha longifolia* extract: synthesis, characterization and antifungal activity. Curr Sci. 2018;114:2116.
107. Ye Y, Xu Y, Liang W, Leung GPH, Cheung KH, Zheng C, et al. DNA-loaded chitosan oligosaccharide nanoparticles with enhanced permeability across Calu-3 cells. J Drug Target. 2013;21:474–86.
108. Lakkakula JR, Matshaya T, Krause RWM. Cationic cyclodextrin/alginate chitosan as 5-fluorouracil drug delivery system. Mater Sci Eng C. 2017;70:169–77.
109. Jhaveri J, Raichura Z, Khan T, Momin M, Omri A. Chitosan nanoparticles-insight into properties, functionalization and applications in drug delivery and theranostics. Molecules. 2021;26:272.

110. Sharma M, Sharma R, Jain DK, Saraf A. Enhancement of oral bioavailability of poorly water soluble carvedilol by chitosan nanoparticles: optimization and pharmacokinetic study. Int J Biol Macromol. 2019;135:246–60.
111. Coutinho AJ, Costa Lima SA, Afonso CMM, Reis S. Mucoadhesive and pH responsive fucoidan-chitosan nanoparticles for the oral delivery of methotrexate. Int J Biol Macromol. 2020;158:180–8.
112. Ahmed T, Aljaeid B. Preparation, characterization, and potential application of chitosan, chitosan derivatives, and chitosan metal nanoparticles in pharmaceutical drug delivery. Drug Des Devel Ther. 2016;483.
113. Wang Y, Pi C, Feng X, Hou Y, Zhao L, Wei Y. The influence of nanoparticle properties on oral bioavailability of drugs. Int J Nanomed. 2020;15:6295–310.
114. Wang J, Yang G, Wang Y, Du Y, Liu H, Zhu Y, et al. Chimeric protein template-induced shape control of bone mineral nanoparticles and its impact on mesenchymal stem cell fate. Biomacromol. 2015;16:1987–96.
115. Ghosh R, Mondal S, Mukherjee D, Adhikari A, Ahmed SA, Alsantali RI, et al. Oral drug delivery using a polymeric nanocarrier: chitosan nanoparticles in the delivery of rifampicin. Mater Adv. 2022;3:4622–8.
116. Kumbhar ST, Patil RY, Bhatia MS, Choudhari PB, Gaikwad VL. Synthesis and characterization of chitosan nanoparticles decorated with folate and loaded with dasatinib for targeting folate receptors in cancer cells. OpenNano. 2022;7:100043.
117. Al-Jbour ND, Beg MDH, Gimbun J, Alam AKMM. Preparation and characterization of low molecular weight chitosan with different degrees of deacetylation by the acid hydrolysis method. Int J Appl Pharm. 2021;153–64.
118. Maćczak P, Kaczmarek H, Ziegler-Borowska M, Węgrzynowska-Drzymalska K, Burkowska-But A. The use of chitosan and starch-based flocculants for filter backwash water treatment. Materials. 2022;15:1056.
119. Buyuk NI, Arayici PP, Derman S, Mustafaeva Z, Yucel S. Synthesis of chitosan nanoparticles for controlled release of amiodarone. Indian J Pharm Sci [Internet]. 2020 [cited 2022 Jul 23];82. Available from: https://www.ijpsonline.com/articles/synthesis-of-chitosan-nanoparticles-for-controlled-release-of-amiodarone-3827.html.
120. Aranda-Barradas ME, Trejo-López SE, Real AD, Álvarez-Almazán S, Méndez-Albores A, García-Tovar CG, et al. Effect of molecular weight of chitosan on the physicochemical, morphological, and biological properties of polyplex nanoparticles intended for gene delivery. Carbohydr Polym Technol Appl. 2022;4:100228.
121. González C, Reyes LH, Muñoz-Camargo C, Cruz JC. Synthesis, characterization, and functionalization of chitosan and gelatin type b nanoparticles to develop novel highly biocompatible cell-penetrating agents. In: 2nd Int Online-Conf Nanomater [Internet]. MDPI; 2020 [cited 2022 Aug 19]. p. 30. Available from: https://www.mdpi.com/2673-4605/4/1/30.
122. Afzali E, Forootanfar H, Eslaminejad T, Amirpour-Rostami S, Ansari M. Enhancing purification of α-amylase by superparamagnetic complex with alginate/chitosan/β-cyclodextrin/TPP. Biocatal Biotransformation. 2019;37:201–9.
123. Alvi Z, Akhtar M, Rahman NU, Hosny KM, Sindi AM, Khan BA, et al. Utilization of gelling polymer to formulate nanoparticles loaded with epalrestat-cyclodextrin inclusion complex: formulation, characterization, in-silico modelling and in-vivo toxicity evaluation. Polymers. 2021;13:4350.
124. Zhang P, Liu X, Hu W, Bai Y, Zhang L. Preparation and evaluation of naringenin-loaded sulfobutylether-β-cyclodextrin/chitosan nanoparticles for ocular drug delivery. Carbohydr Polym. 2016;149:224–30.
125. Anter HM, Abu Hashim II, Awadin W, Meshali MM. Novel chitosan oligosaccharide-based nanoparticles for gastric mucosal administration of the phytochemical "apocynin." Int J Nanomed. 2019;14:4911–29.
126. Alizadeh N, Nazari F. Thymol essential oil/ β-cyclodextrin inclusion complex into chitosan nanoparticles: improvement of thymol properties in vitro studies. J Mol Liq. 2022;346: 118250.
127. Zhu W, Wu J, Guo X, Sun X, Li Q, Wang J, et al. Development and physicochemical characterization of chitosan hydrochloride/sulfobutyl ether-β-cyclodextrin nanoparticles for cinnamaldehyde entrapment. J Food Biochem [Internet]. 2020 [cited 2022 Jun 26];44. Available from: https://onlinelibrary.wiley.com/doi/10.1111/jfbc.13197.
128. Hanafy AS, Farid RM, ElGamal SS. Complexation as an approach to entrap cationic drugs into cationic nanoparticles administered intranasally for Alzheimer's disease management: preparation and detection in rat brain. Drug Dev Ind Pharm. 2015;41:2055–68.
129. Tong QP, Sun HS, Wang J, Wang Y, Peng Y, Jiang M, et al. Preparation and characterization of berberine hydrochloride and trimethoprim chitosan/SBE7-β-CD microspheres. J Drug Deliv Sci Technol. 2018;48:300–10.
130. Zhao L, Tang B, Tang P, Sun Q, Suo Z, Zhang M, et al. Chitosan/sulfobutylether-β-cyclodextrin nanoparticles for ibrutinib delivery: a potential nanoformulation of novel kinase inhibitor. J Pharm Sci. 2020;109:1136–44.
131. Karpkird T, Manaprasertsak A, Penkitti A, Sinthuvanich C, Singchuwong T, Leepasert T. A novel chitosan-citric acid crosslinked beta-cyclodextrin nanocarriers for insoluble drug delivery. Carbohydr Res. 2020;498:108184.
132. Jafar M, Khalid MS, Alghamdi H, Amir M, Al Makki SA, Alotaibi OS, et al. Formulation of apigenin-cyclodextrin-chitosan ternary complex: physicochemical characterization, in vitro and in vivo studies. AAPS PharmSciTech. 2022;23:71.
133. Sadaquat H, Akhtar M, Nazir M, Ahmad R, Alvi Z, Akhtar N. Biodegradable and biocompatible polymeric nanoparticles for enhanced solubility and safe oral delivery of docetaxel: in vivo toxicity evaluation. Int J Pharm. 2021;598:120363.
134. Alizadeh N, Malakzadeh S. Antioxidant, antibacterial and anticancer activities of β-and γ-CDs/curcumin loaded in chitosan nanoparticles. Int J Biol Macromol. 2020;147:778–91.
135. Akbar N, Kawish M, Khan NA, Shah MR, Alharbi AM, Alfahemi H, et al. Hesperidin-, curcumin-, and amphotericin B-based nano-formulations as potential antibacterials. Antibiotics. 2022;11:696.
136. Joshi S, Dhingra AK, Chopra B, Dass R, Guarve K, Sapra S. Formulation and evaluation of solid dispersions of poorly water-soluble drug- hesperidin. Lett Appl NanoBioScience. 2022;12:50.
137. Kalita B, Patwary BN. Formulation and in vitro evaluation of hesperidin-phospholipid complex and its antioxidant potential. Curr Drug Ther. 2020;15:28–36.
138. Sadaquat H, Akhtar M. Comparative effects of β-cyclodextrin, HP-β-cyclodextrin and SBE7-β-cyclodextrin on the solubility and dissolution of docetaxel via inclusion complexation. J Incl Phenom Macrocycl Chem. 2020;96:333–51.
139. Sakran W, Safa R, Abdel-Hakim M, Salah M. Investigation and physicochemical characterization of binary febuxostat- sulfobutyl ether β -cyclodextrin inclusion complexes. J Adv Pharm Res. 2022;0:0–0.
140. Li S, Shi W, Wang X, Hu X, Li S, Zhang Y. The preparation and characterization of electrospun gelatin nanofibers containing chitosan/eugenol-sulfobutyl-β-cyclodextrin nanoparticles. Colloids Surf Physicochem Eng Asp. 2022;648:129109.
141. Wdowiak K, Rosiak N, Tykarska E, Żarowski M, Płazińska A, Płaziński W, et al. Amorphous inclusion complexes: molecular

interactions of hesperidin and hesperetin with HP-B-CD and their biological effects. Int J Mol Sci. 2022;23:4000.
142. Wdowiak K, Walkowiak J, Pietrzak R, Bazan-Woźniak A, Cielecka-Piontek J. Bioavailability of hesperidin and its aglycone hesperetin—compounds found in citrus fruits as a parameter conditioning the pro-health potential (neuroprotective and antidiabetic activity)—mini-review. Nutrients. 2022;14:2647.
143. Shukla SK, Chan A, Parvathaneni V, Kanabar DD, Patel K, Ayehunie S, et al. Enhanced solubility, stability, permeation and anticancer efficacy of celastrol-β-cyclodextrin inclusion complex. J Mol Liq. 2020;318:113936.
144. Parvathaneni V, Elbatanony RS, Goyal M, Chavan T, Vega N, Kolluru S, et al. Repurposing bedaquiline for effective non-small cell lung cancer (NSCLC) therapy as inhalable cyclodextrin-based molecular inclusion complexes. Int J Mol Sci. 2021;22:4783.
145. Aman RM, Zaghloul RA, El-Dahhan MS. Formulation, optimization and characterization of allantoin-loaded chitosan nanoparticles to alleviate ethanol-induced gastric ulcer: in-vitro and in-vivo studies. Sci Rep. 2021;11:2216.
146. Elmowafy E, El-Derany MO, Casettari L, Soliman ME, El-Gogary RI. Gamma oryzanol loaded into micelle-core/chitosan-shell: from translational nephroprotective potential to emphasis on sirtuin-1 associated machineries. Int J Pharm. 2023;631:122482.
147. Mura P, Maestrelli F, Cirri M, Mennini N. Multiple roles of chitosan in mucosal drug delivery: an updated review. Mar Drugs. 2022;20:335.
148. Varela-Fernández R, García-Otero X, Díaz-Tomé V, Regueiro U, López-López M, González-Barcia M, et al. Design, optimization, and characterization of lactoferrin-loaded chitosan/TPP and chitosan/sulfobutylether-β-cyclodextrin nanoparticles as a pharmacological alternative for keratoconus treatment. ACS Appl Mater Interfaces. 2021;13:3559–75.
149. Sohel M, Sultana H, Sultana T, Al Amin Md, Aktar S, Ali MdC, et al. Chemotherapeutic potential of hesperetin for cancer treatment, with mechanistic insights: a comprehensive review. Heliyon. 2022;8:e08815.
150. Xia R, Xu G, Huang Y, Sheng X, Xu X, Lu H. Hesperidin suppresses the migration and invasion of non-small cell lung cancer cells by inhibiting the SDF-1/CXCR-4 pathway. Life Sci. 2018;201:111–20.
151. Yang Z, Yang H, Dong X, Pu M, Ji F. Hesperidin loaded Zn2+@SA/PCT nanocomposites inhibit the proliferation and induces the apoptosis in colon cancer cells (HCT116) through the enhancement of pro-apoptotic protein expressions. J Photochem Photobiol B. 2020;204:111767.
152. Bagher Z, Ehterami A, Nasrolahi M, Azimi M, Salehi M. Hesperidin promotes peripheral nerve regeneration based on tissue engineering strategy using alginate/chitosan hydrogel: *in vitro* and *in vivo* study. Int J Polym Mater Polym Biomater. 2021;70:299–308.
153. Gadade DD, Pekamwar SS. Cyclodextrin based nanoparticles for drug delivery and theranostics. Adv Pharm Bull. 2020;10:166–83.
154. Li Y, Kandhare AD, Mukherjee AA, Bodhankar SL. Acute and sub-chronic oral toxicity studies of hesperidin isolated from orange peel extract in Sprague Dawley rats. Regul Toxicol Pharmacol. 2019;105:77–85.
155. Soe HMSH, Luckanagul JA, Pavasant P, Jansook P. Development of in situ gel containing asiaticoside/cyclodextrin complexes. Evaluation in culture human periodontal ligament cells (HPLDCs). Int J Pharm. 2020;586:119589.
156. Mukhtar M, Fényes E, Bartos C, Zeeshan M, Ambrus R. Chitosan biopolymer, its derivatives and potential applications in nano-therapeutics: a comprehensive review. Eur Polym J. 2021;160:110767.
157. Sheikh A, Md S, Alhakamy NA, Kesharwani P. Recent development of aptamer conjugated chitosan nanoparticles as cancer therapeutics. Int J Pharm. 2022;620:121751.
158. Xu D, Li X, Huang Y, Tang Z, Ran C, Jing B, et al. Preparation, characterization and pharmacokinetic studies of sulfobutyl ether-β-cyclodextrin-toltrazuril inclusion complex. J Mol Struct. 2021;1223:128969.
159. Guo W, Yi L, Zhou B, Li M. Chitosan modifies glycemic levels in people with metabolic syndrome and related disorders: meta-analysis with trial sequential analysis. Nutr J. 2020;19:130.
160. Liu SH, He SP, Chiang MT. Effects of long-term feeding of chitosan on postprandial lipid responses and lipid metabolism in a high-sucrose-diet-impaired glucose-tolerant rat model. J Agric Food Chem. 2012;60:4306–13.
161. Saharan P, Bahmani K, Saharan SP. Preparation, optimization and in vitro evaluation of glipizide nanoparticles integrated with Eudragit RS-100. Pharm Nanotechnol. 2019;7:72–85.
162. Stella VJ, Rajewski RA. Sulfobutylether-β-cyclodextrin. Int J Pharm. 2020;583:119396.